Acta Geotechnica (2022) 17:2971–2994
https://doi.org/10.1007/s11440-021-01426-z

RESEARCH PAPER

Alternant active and passive trapdoor problem: from experimental investigation to mathematical modeling

Yaojie Wu[1,2] · Yu Zhao[1,2] · Quanmei Gong[1,2] · Jorge G. Zornberg[3] · Shunhua Zhou[1,2] · Binglong Wang[1,2]

Received: 26 July 2020 / Accepted: 24 November 2021 / Published online: 16 December 2021

Abstract

In the classical conception of the arching mechanism, the well-known trapdoor problem assumes distinctive modes (e.g., either active or passive mode) in the original geostatic overburden pressure. However, in various geotechnical applications, underground inclusions or structures may experience alternant upward and downward movements induced by construction activities or environmental changes, leading the ground to be initial loss or compaction state. If the initial disturbed state occurs, the estimation of vertical load on structures is improper based on classical trapdoor mechanism. In this study, a new conception, alternant active and passive trapdoor problem was introduced. Using a comprehensive measured system, such as particle image velocity technique and various sensors, alternant active and passive trapdoor tests were conducted to explore the mechanical behavior and kinematic mechanism of the backfill subjected to continuous loading and unloading. The development of arching with trapdoor displacement was visualized and quantified in different modes and states. Then, this problem was treated in a statical analysis based upon the visualized kinematic mechanisms. Solutions for the trapdoor load in the typical development states of arching were calculated by limit equilibrium method. Finally, two simplified ground reaction curves representing the progressive development of arching were proposed to facilitate in engineering applications. The simplified method was verified by the trapdoor test results.

Keywords Arching effect · Ground disturbance · Kinematic mechanism · Mechanical behavior · Trapdoor test

List of symbols

B	Trapdoor width
H	Thickness of sand bed
L	Trapdoor length
i	H/B, Embedment ratio of trapdoor
s	Displacement of trapdoor
s_{max}	Maximum displacement of trapdoor
δ	Normalized displacement of trapdoor (by B), δ_x = normalized displacement corresponding to specific stage (x = A, B, C, D, F, H, b, d, g, h, i)
δ_{max}	Maximum normalized displacement of trapdoor
δ_{min}	Normalized displacement corresponding to the maximum arching
v	Moving speed of trapdoor
n	Number of cycles of trapdoor movement
D_r	Relative compactness of sand
φ	Friction angle of sand
φ_p	Peak friction angle of sand
φ_{cri}	Critical friction angle of sand
ψ	Dilation angle of sand
θ	The inclination angles of slip surface (measured between the vertical direction and the slip surface)
γ	Unit weight of sand
ρ	Normalized load on trapdoor (by γBHL), or arching ratio, ρ_x = normalized load at specific stage (x = A, B, C, D, F, H, b, d, g, h, i)

✉ Yu Zhao
yuzhao@tongji.edu.cn

[1] Key Laboratory of Road and Traffic Engineering of the Ministry of Education, Tongji University, Shanghai 201804, China

[2] Shanghai Key Laboratory of Rail Infrastructure Durability and System Safety, Tongji University, Shanghai 201804, China

[3] Department of Civil, Architectural and Environmental Engineering, The University of Texas at Austin, Texas 78712-0273, USA

P_x	Load per unit length on the trapdoor at specific stage (x = A, B, C, D, F, H, b, d, g, h, i)
S^{i}	Incremental displacement of granular body
Sc	Cumulative surface upheaval
σ_{f}	Measured soil stress
σ_{i}	Initial measured soil stress
σ_{x0}	Initial horizontal stress
σ_{z0}	Initial vertical stress
K_0	σ_{x0}/σ_{z0}, Initial lateral earth pressure coefficient
σ_x	Horizontal stress
σ_z	Vertical stress
σ_n	Normal stress on the slip plane
K	σ_x/σ_z, Modified lateral earth pressure coefficient related to arching ratio
K_{h}	σ_n/σ_z, Ratio of normal stress to vertical stress
K_{E}	$(1 - \sin^2\varphi)/(1 + \sin^2\varphi)$, a ratio of the vertical stress to the horizontal stress based on an inclined shearing surface [25]
K_{D}, K_{H}	Lateral earth pressure coefficient at specific stage (i.e., at point D, H)
p	Stress level or confining stress
σ_z	The vertical stress at a depth z below the ground level

1 Introduction

Soil arching, a ubiquitous phenomenon in soil–structure interaction problems in civil and mining engineering, is defined as the transfer of load between a moving soil mass and an adjacent stationary mass [44]. It is extensively used to estimate the vertical load or limit support pressure in the design of tunnels [7, 8, 30, 31, 33, 34], pile-supported embankments [22, 35, 46], underground pipelines [10, 11, 39, 47] and other buried structures [9, 36, 38]. According to the direction of relative displacement between soil and structure, two types of arching effect are identified, namely active and passive arching [25, 27]. Since the trapdoor test was performed by Terzaghi to experimentally investigate the arching effect [43, 44], numerous extensions of this method have been performed in physical laboratory experiments [3, 6, 13, 18, 24, 26, 28, 30, 45, 53]. In these studies of the "trapdoor mechanism'", the focus was on investigating monotonic modes of arching (e.g., active or passive arching), assuming that the soil was in the original geostatic stress state before test without considering previous disturbed state of soil. However, construction activities (e.g., tunneling, grouting) or the change and erosion of environment (e.g., karstic collapse, soil dissolution, rock weathering, freezing and thawing) inevitably disturbed the ground, changing the stress state and mechanical properties of soils, and ground loss or elevation may occur continuously. For instance, when machines or structures are buried in different and complex environments, the state of the ground is inevitably disturbed by various engineering activities and environmental changes throughout their entire life cycle. Buried machines may move downward or upward to seek for optimal attitude during construction (e.g., a buried shield machine) [50, 51]. The buried structures unexpectedly built above expansive soil, seasonal frozen soil or rock layer may undergo upward and downward movement within its service life [42]. A tunnel suffering from differential settlement may be uplifted to the original position by grouting technology to satisfy the operation safety [21, 54]. Suffering from some accidents (e.g., ground subsidence, leakage), the subsided drainage pipelines need to be restored and uplifted using the polymer grouting technology for its long-term operation [17, 19]. The anchor to support offshore floating energy converters inevitably bears wave cyclic load in the whole life cycle [15, 32]. The buried power transferring pipeline subjected to high pressure and temperature may be relieved by upheaval buckling and offset the original position [11, 39]. Obviously, all of these activities and environmental changes may lead continuous disturbance to the soil, significantly affecting the state and deformation of the ground.

When the ground suffered from continuous disturbances induced by alternant downward and upward movement, the initial stress state of the adjacent soil will be affected as the redistribution of stress related to ground deformation occurred. The relative density of soil will change after the previous disturbance, which significantly affects the strength-deformation properties and the degree of particle interlocking [20, 37]. Load evolution and load transfer mechanisms are thus affected [2, 56]. More importantly, the simple pattern of either active or passive mode of arching is not applicable to estimate the load considering the ground disturbance generated by the buried machines or structures undergo alternating and even cyclic upward and downward movements. To address these issues, it is necessary to extend the exploration of the arching phenomenon beyond the rather narrow traditional perspective of monotonic loading vs. displacement patterns. Then, a new conception, a broader framework of alternant active and passive arching modes has been conceived by Zhao et al. [52].

The alternant active and passive trapdoor problem was first investigated by Aqoub et al. [1]. This study mainly focused on the load evolution of sequential active and passive arching and found that the alternation of the movement direction was detrimental to formation of full

active and passive arching. However, just depending on the mechanical behavior, the deformation behavior of backfill was not investigated and it cannot give a recognized and reasonable interpretation for the development of arching in the soil subjected to alternant active and passive trapdoor. Recently, Zhao et al. [52] investigated the deformation behavior and identified the typical progressive failure modes in the soil under alternant active and passive conditions using a particle image velocity system. However, more attention focused on the comparison of the kinematic characteristic in granular sand and load evolution on trapdoor between alternating active or passive arching and the initial active or passive arching (i.e., classical active or passive arching). Overall, these two studies paid more focus on the description of experimental phenomena. More remaining problems, such as mechanical behavior of trapdoor and kinematic mechanism of backfill, need to be further investigated. Besides, it only stays in the qualitative analysis and cannot carry out the quantitative calculation for guiding the load estimation in engineering applications.

This study investigates the alternant active and passive trapdoor problem under plane strain condition, focusing on mechanical behavior and failure mechanism. A trapdoor apparatus was utilized with a series of sensors and high-speed imaging equipment to acquire the load on trapdoor and capture the sand displacement. Comprehensive investigation aims to (i) analyze the mechanical behavior and failure mechanism of arching under alternant active and passive trapdoor condition, (ii) quantify the load exerted on trapdoor, (iii) investigate the effect of moving speed and magnitude of trapdoor displacement on the development of arching, and (iv) propose a simplified method to estimate the vertical load on buried machines/structures based on the kinematic characteristic in granular backfill. This study visualized deformation behavior in granular sand and quantified load exerted on trapdoor with alternating active and passive movements, which provide some practical implications on evaluating the local ground subsidence or uplift behavior and predicting the life-cycle load on underground infrastructures.

2 Experimental investigation

2.1 Methods

2.1.1 Testing equipment

The test equipment consists of a trapdoor apparatus and a comprehensive measured system, as shown in Fig. 1a. The inner dimensions of the transparent container are 700 mm in length, 300 mm in width and 700 mm in height, whereas the width of trapdoor B is 150 mm, as illustrated in Fig. 1b. The trapdoor apparatus is large enough to mitigate the boundary effect on the sensors' readings. A fibre seal covers all four edges of the trapdoor to minimize frictional resistance and to prevent ingress of granular materials between the trapdoor edges and the fixed side walls. The gap between the edge of trapdoor and the stationary part is less than 0.1 mm, which is smaller than the particle size of prepared sand. Controlled by the motor system, the speed of the trapdoor can be adjusted from 0.1 to 20 mm/min with an accuracy of 0.02 mm/min. The comprehensive measurement system including transducers and the corresponding data acquisition as well as a self-developed particle image velocimetry (PIV) system, is introduced in detail below. (i) The displacement of the trapdoor was monitored by placing a linear variable pull rope displacement transducer (DT) with the range of 35 mm under the trapdoor. DT was connected to a data acquisition device (DAQ). (ii) A load transducer (LT), calibrated to force range from 0 to 2000 N by the manufacturer, was mounted to the base of the trapdoor to measure the applied load on the trapdoor. (iii) Three high-precision laser displacement sensors (LDS) with the range of 30 mm were installed to track the surface settlement during movement of the trapdoor. LDS-1, 2, 3 were spaced equally at 63 mm intervals, and the left one (LDS-1) was in line with the trapdoor centerline. (iv) Eight soil stress transducers (SST) were placed horizontally at different heights on one side of the soil box according to symmetry. The location of SST is illustrated in Fig. 1c. SST-1, 2, 3 were placed on the trapdoor and the center of SST-1 coincided with the center of the trapdoor. SST-4, 5 were on the stationary part spaced at 60 mm intervals. SST-6, 7, 8 were placed 100 mm above the trapdoor and the stationary part, coinciding with SST-1, 4, 5, respectively. All the SST were calibrated in sand body or rigid base before the tests, depending on the location. Detailed calibration methods referred to the method proposed by Zhu et al. [55]. (v) Based on the series studies by the authors, a self-developed PIV system was developed to capture the soil displacement, which will provide considerable insights into the evolution of deformations within the soil subjected to alternant active and passive movements. The specific details of the PIV system can be found in Gong et al. [21] and Zhao et al. [53]. Data acquisition frequency in this study is 2 Hz. All the collected data were displayed on the computer screen in real time.

2.1.2 Backfill properties

Commercial quartz sand was selected as experimental material. The sieve analysis of the sand shows that 95% of the particle were in the range of 0.5 to 1 mm. The specific gravity G_s = 2.186, the coefficient of curvature C_c = 0.99 and the coefficient of uniformity C_u = 1.42. Other

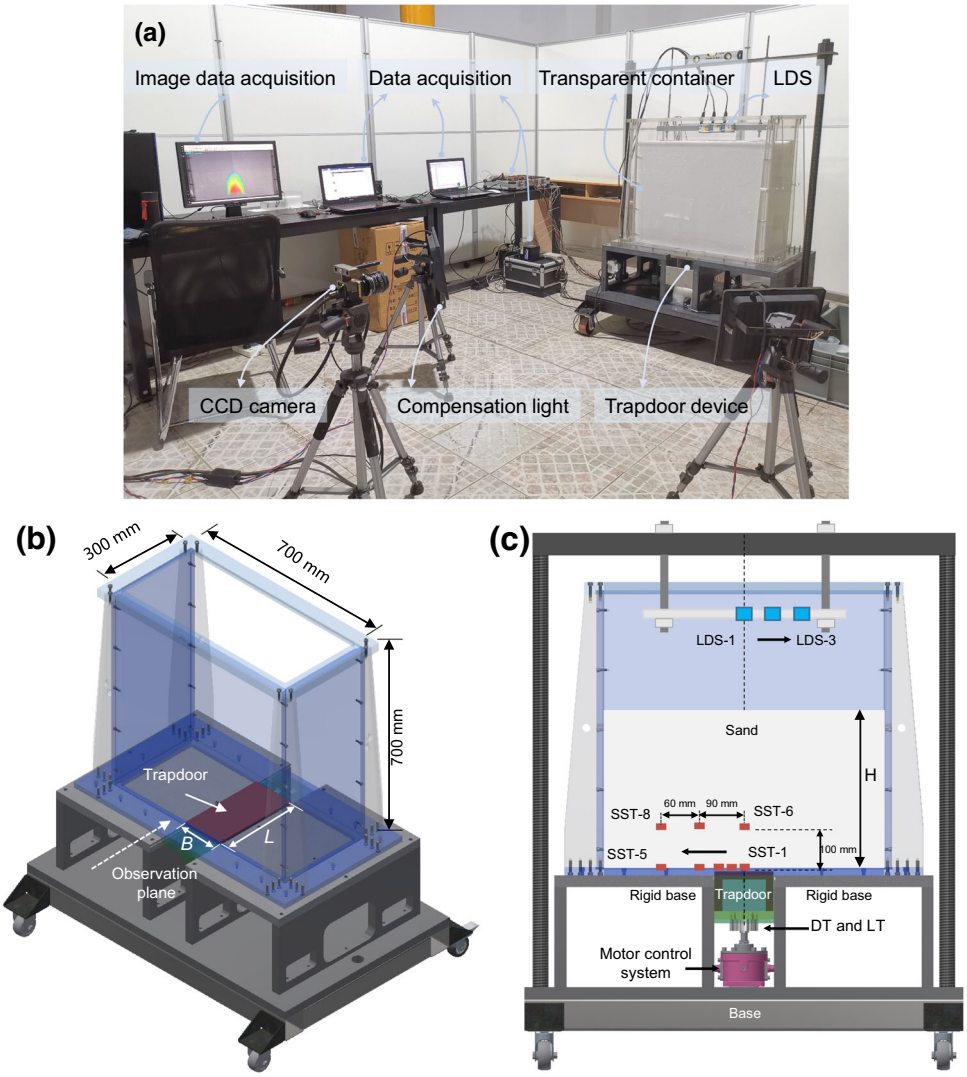

Fig. 1 Model test equipment for laboratory investigation: **a** Model test setup; **b** Trapdoor apparatus (**a** and **b** from Zhao et al. [53]; with permission); **c** Front view and layout of sensors

important index properties were D_{50} = 0.7 mm, ρ_{max} = 1.286 g/cm^3 and ρ_{min} = 1.030 g/cm^3, D_r = 60%. Determined by axisymmetric triaxial tests, the peak friction angle φ_p and the critical friction angle φ_{cri} were equal to 45.6° and 42.5° at D_r of 60%, respectively. The dilation angel ψ were equal to 20.6°, 16.2° and 14.1° at confining stress of 30 kPa, 50 kPa and 70 kPa, respectively. The tests were conducted under dry sand condition and the results will be compared to those tests conducted in saturated quartz with liquid mixture of oil (i.e., artificial transparent sand) in the future study.

2.1.3 Experimental procedure

To attain a uniform density of sand in the container and avoid a discrepancy in the surface settlement measurements, the sand container was filled in layers approximately 5 mm thick until reaching the required height by the air pluviation method [29]. Most tests were initiated by moving the trapdoor downward or upward at a constant speed of 2.0 mm/min to a predetermined normalized displacement δ (normalized by the width of trapdoor B, e. g., trapdoor displacement s_{max} = 30.0 mm, B = 150.0 mm, and $\delta_{max} = s_{max}/B$ = 20%). In this paper, δ is defined as the normalized displacement relative to the initial position of the trapdoor. When the trapdoor moves upward from the initial position for initial passive mode, δ is considered to be positive. On the contrary, δ is considered to be negative. This step achieves active or passive state as classical trapdoor tests under initial stress state. After a temporary stop, the movement direction of the trapdoor was reversed to perform the opposite state of arching. The subsequent movement followed the same procedure. For each subsequent movement, the previous

movements can be regarded as the ground disturbance (e.g., ground loss or elevation). Each test was conducted to simulate three to six cycles of alternating movement. As tabulated in Table 1, eight tests were performed. According to the initial movement direction of the trapdoor, it was divided into initial passive mode (i.e., initial ground elevation) and initial active mode (i.e., initial ground loss). The embedment ratio i is defined as the ratio of the thickness of sand bed H to the trapdoor width B. Each series of tests was conducted with four i (i.e., i = 1, 2, 3 and 4). Besides, the effect of the magnitude of trapdoor displacement was investigated in Test I-3, and the effect of number of cycles was explored in Test I-4. While, the effect of moving speed of trapdoor was studied in Test II-4. The results of initial passive mode and initial active mode are presented in Sects. 2.2 and 2.3, respectively.

2.2 Results of initial passive mode

The load–displacement responses of initial passive mode are presented in Fig. 2. Just like δ, the normalized load ρ (i.e., arching ratio) was defined as the ratio of the net load F by the original self-weight value F_0. The load evolution of initial passive mode was divided into initial cycle and subsequent cycle.

2.2.1 Initial cycle

Initial cycle can be divided into two specific states: initial passive state (IP) and subsequent active state (SA-IP). To describe the development of arching in the initial cycle, several transitional phases or feature points are selected and defined in Fig. 3. Feature points A, B and C represent the break point of load displacement curve, maximum load, and ultimate load, respectively. For SA-IP, feature points D and E represent the two break points of load displacement curve. Whereas, point F is transitional phase and can be called as fully mobilized arching stage, where the trapdoor carries relatively small load. Point K can be called as ultimate state.

For the IP, the load–displacement curve was just as monotonic passive arching in classical trapdoor test. When the trapdoor moved upwards, the arching load gradually increased to a peak value as the part of soil around the trapdoor mobilized shear strength. At this time, the load on stationary regions transferred to the trapdoor. With the trapdoor moving further, there was no significant reduction in load on the trapdoor, which means that there was no obvious stress-softening behavior in quartz sand. Incremental displacement S^i in the end of initial stage (Fig. 3A), maximum passive arching (Fig. 3B) and ultimate state (Fig. 3C) are presented in Fig. 4. Zhao et al. [52] studied the effect of trapdoor buried depth and found that regarding as the evolution of failure zone, there is no significant difference between shallow and deep conditions. Hence, only S^i at i of 3 was presented typically to short the text. S^i plots show the change between the current image and the previous image with a trapdoor displacement step of 3.33 mm (1 or 1.5 mm for initial stage). It shows that there was approximately a rectangular influence zone in the initial stage (Fig. 4A). As the trapdoor uplifted further, an inverted trapezoid or trumpet influence zone was observed in both maximum resistance (Fig. 4B) and ultimate state (Fig. 4C).

Reversing the trapdoor led to the SA-IP. As the trapdoor moved downwards, the load on the trapdoor decreased monotonically, which was significantly different from that of classical active trapdoor test. In classical active arching load, a load drop can be recorded firstly with a relatively small displacement, followed by a load recovery stage [23]. According to selected feature points (D, E and F), the load evolution of SA-IP was divided into four typical phases in Fig. 3, including initial stage (O ∼ D), convergence stage (D ∼ E), full mobilized arching stage (E ∼ F), and ultimate state (K).

Table 1 Summary of tests performed

Series	Mode	Tests	i (H/B)	Number of cycles n	Maximum normalized displacement δ (%)	Moving speed v (mm/min)
I	Initial passive mode	I-1	1	$n = 3$	$\delta_{1\sim3} = 20$	$v_{1\sim3} = 2$
		I-2	2	$n = 3$	$\delta_{1\sim3} = 20$	$v_{1\sim3} = 2$
		I-3	3	$n = 5$	$\delta_{1\sim3} = 20$, $\delta_4 = 13.333$, $\delta_5 = 6.667$	$v_{1\sim5} = 2$
		I-4	4	$n = 6$	$\delta_{1\sim6} = 20$	$v_{1\sim6} = 2$
II	Initial active mode	II-1	1	$n = 3$	$\delta_{1\sim3} = -20$	$v_{1\sim3} = 2$
		II-2	2	$n = 3$	$\delta_{1\sim3} = -20$	$v_{1\sim3} = 2$
		II-3	3	$n = 3$	$\delta_{1\sim3} = -20$	$v_{1\sim3} = 2$
		II-4	4	$n = 5$	$\delta_{1\sim5} = -20$	$v_{1\sim3} = 2$, $v_4 = 10$, $v_5 = 20$

δ_j: predetermined normalized displacement (j = 1, …, n, where j represents corresponding cycle), v_j: movement speed of the trapdoor

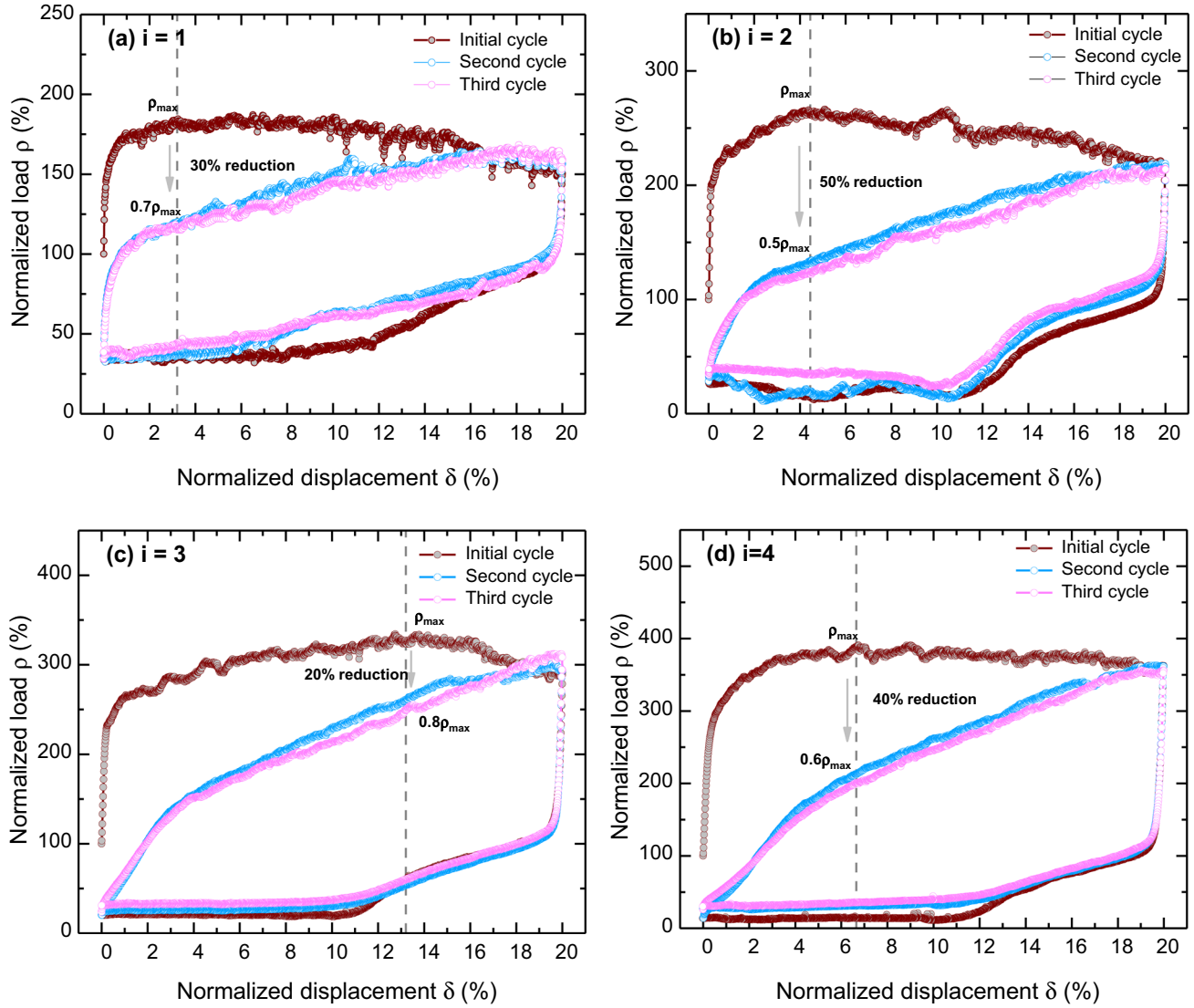

Fig. 2 Load–displacement curves for initial passive mode in different embedment ratios

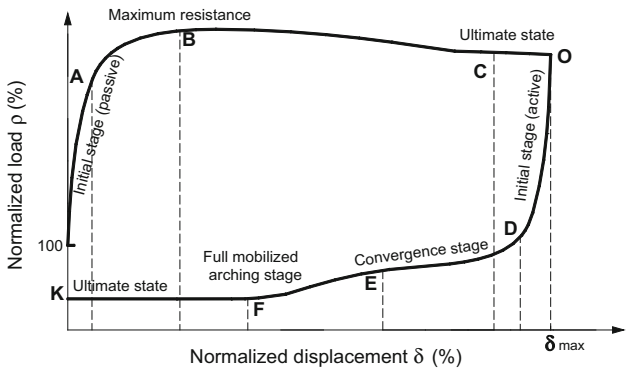

Fig. 3 Typical phases of load–displacement curve for the initial cycle of initial passive mode

S^i at selected feature points are presented in Fig. 5. An inverted trapezoidal influence zone was observed in the initial stage (Fig. 5D) that followed the previous influence zone (Fig. 4C). With the trapdoor yielding further, the area of influence started contracting inward and downward in the convergence stage (Fig. 5E). Surface upheaval along the centerline of the trapdoor (recorded by LDS-1) in Fig. 6 illustrated that the rate of surface settlement slowed down and the cumulative upheaval gradually stabilized, no longer decreasing rapidly with the development of arching (Fig. 5F). A parabolic-shaped area was highlighted above the trapdoor due to the significantly large incremental displacement in the ultimate state (Fig. 5K), which can be defined as the *arch of equal displacement* [27] (i.e., equal displacement region as the trapdoor). The cumulative upheaval S^p after a cycle of upward and downward

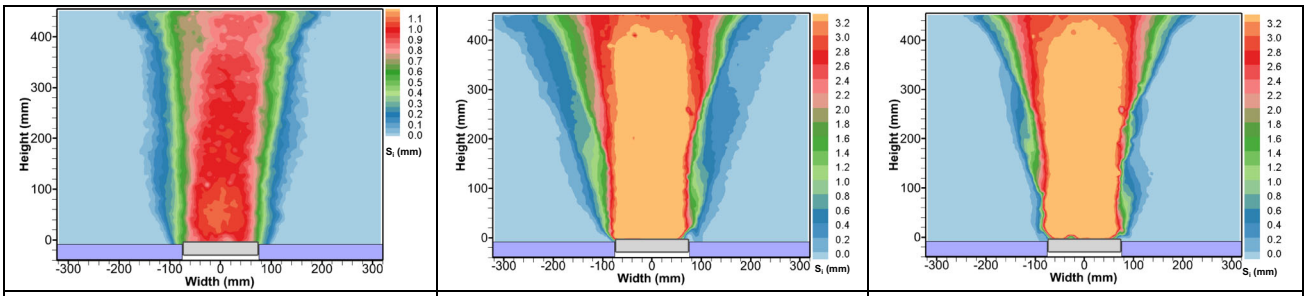

(A) Initial stage (s = 1.5; mm δ = 1%;Point A) | **(B)** Maximum resistance (s = 20 mm; δ = 13.3%;Point B) | **(C)** Ultimate state (s = 26.7 mm; δ = 17.8%; Point C)

Fig. 4 Incremental displacement in typical stages in the IP (Note: unit: mm; points **A**, **B** and **C** are marked in Fig. 3)

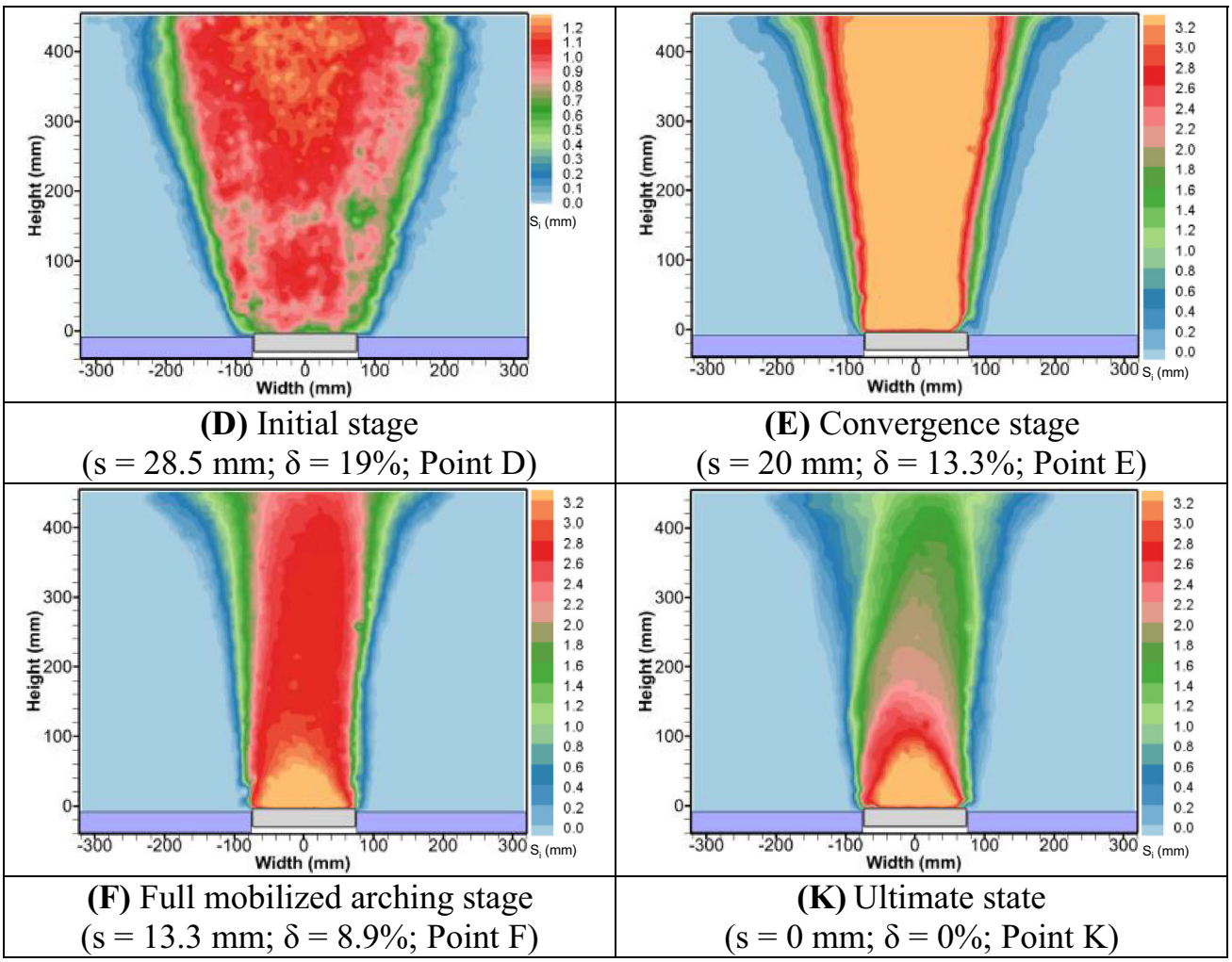

(D) Initial stage (s = 28.5 mm; δ = 19%; Point D) | **(E)** Convergence stage (s = 20 mm; δ = 13.3%; Point E)

(F) Full mobilized arching stage (s = 13.3 mm; δ = 8.9%; Point F) | **(K)** Ultimate state (s = 0 mm; δ = 0%; Point K)

Fig. 5 Incremental displacement in typical stages in the SA-IP (Note: unit: mm; points **D**, **E**, **F**, and **K** are marked in Fig. 3)

movement in Fig. 6 indicates that the sand became loose, and the ground disturbance occurred.

Remarkably, there are two load drops in initial stage (O ∼ D) and full mobilized arching stage (E ∼ F). Before trapdoor receded in point O, the uplifted failure wedge is subject to downward friction along the boundary of failure zone. As the trapdoor moves down, the direction of friction on the boundary surface of the failure zone gradually changed from downward to upward in stage of O ∼ D. This resulted in the sharper load transfer (even over than 100%) in initial stage (O ∼ D) than stage of E ∼ F. Whereas, the failure mechanism in full mobilized arching

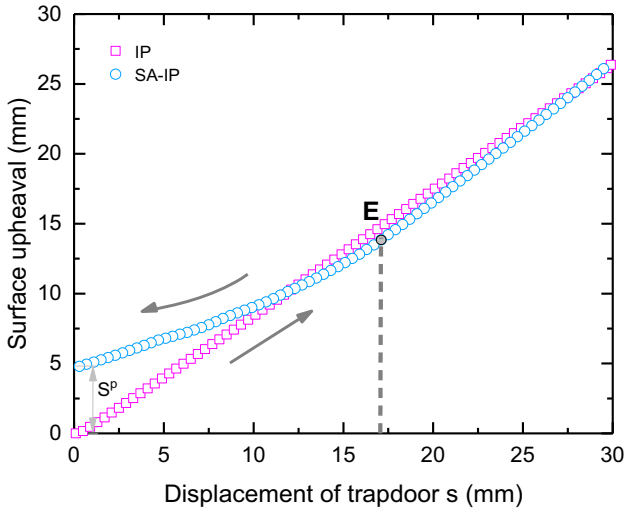

Fig. 6 Surface upheaval along the centerline of the trapdoor (recorded by LDS-1) in the initial cycle of initial passive mode at *i* of 3

stage (E ∼ F) should be similar as classical arching mechanism. This indicates that the initial passive disturbance (i.e., elevation for trapdoor squeezing the sand) had a great influence on the load evolution of the sand above the trapdoor.

2.2.2 Subsequent cycle

When the trapdoor was uplifted again for the subsequent passive state (SP-IP), the load above the trapdoor increased monotonically with the uplift of the trapdoor. Three typical phases, including initial stage (K ∼ H), outspread stage (H ∼ J) and ultimate state (J ∼ O), are defined in Fig. 7. Initial stage presents linear feature of load–displacement response. Point H can be defined as elastic limit point. Whereas, point J would be ultimate state. Points G and I are intermediate phase.

S^i at selected points are shown in Fig. 8. It is evident that an approximately parabolic area with significantly larger

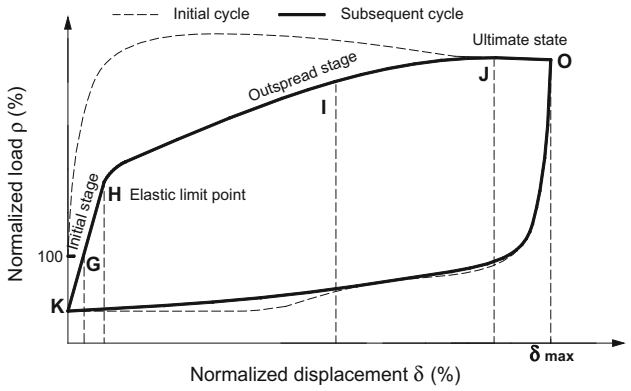

Fig. 7 Typical phases of load–displacement curve for the subsequent cycle of initial passive mode

incremental displacement than surrounding area formed in the initial stage (Fig. 8G). Records of surface upheaval in Fig. 9 also indicates that no surface upheaval appeared in this stage. Because the soil mass above the trapdoor became loose after the initial cycle of movement (see Fig. 6), local punching shear failure occurred at this stage. Hence, it can be regarded as a densifying phase. Then, the influence zone gradually extended upwards toward the surface with the shape of the zone changing from a parabola to a rectangle (Fig. 8H). After the influence zone reached ground surface, the upper part of influence zone expanded horizontally and changed from rectangular to an inverted isosceles trapezoid shape (Fig. 8I). And the surface upheaval (recorded by LDS-1, 2 and 3) started increasing with the uplift of the trapdoor in the outspread stage (Fig. 9H–J). Finally, the surface upheaval increased steadily in the ultimate state (Fig. 9J–O). Figure 8J exhibited an inverted isosceles trapezoid influence zone, which was similar to the situation in the ultimate state of IP (Fig. 4C). Meanwhile, the load in the ultimate state (Fig. 7J) was roughly equal to the ultimate load in the IP (Fig. 3C). For SP-IP, the load–displacement curve in exhibits a monotonical increase of trend until ult state. However, for IP, the load quickly increased to peak and then decreased to an ultimate load. Besides, at δ corresponding to the peak resistance in the IP, it is worth noting that the ρ recorded approximately 20% to 50% reduction for SP-IP, as shown in Fig. 2. However, both two states reach the same final ultimate load. The sand density is the main factor to cause the difference of curve performance between IP and SP-IP. The different trends can also be inferred from the known stress–strain response of sand; high density is associated with a stiff shear resistance to peak strength and subsequent strain softening, whereas low density has lower stiffness and exhibits strain hardening.

Reversing the direction of the trapdoor to achieve another subsequent active state, the load–displacement curve presented a similar tendency as the previous SA-IP; hence, it will not be discussed in detail. Load–displacement curve of the third cycle presented almost coincident paths with that of the second cycle.

2.2.3 Effect of number of cycles

To further investigate the stress state of sand body subjected to continuous loading and unloading, test I-4 with 6 cycles was conducted and the results are shown in Fig. 10. It can be observed that with the increase in number of cycles, the load–displacement curve in the subsequent cycles, though significantly deviates from that in the initial cycle, followed an almost coincident load–displacement path with second cycle, whereas a slightly hysteresis phenomenon can be observed. Analogous to the concept of the

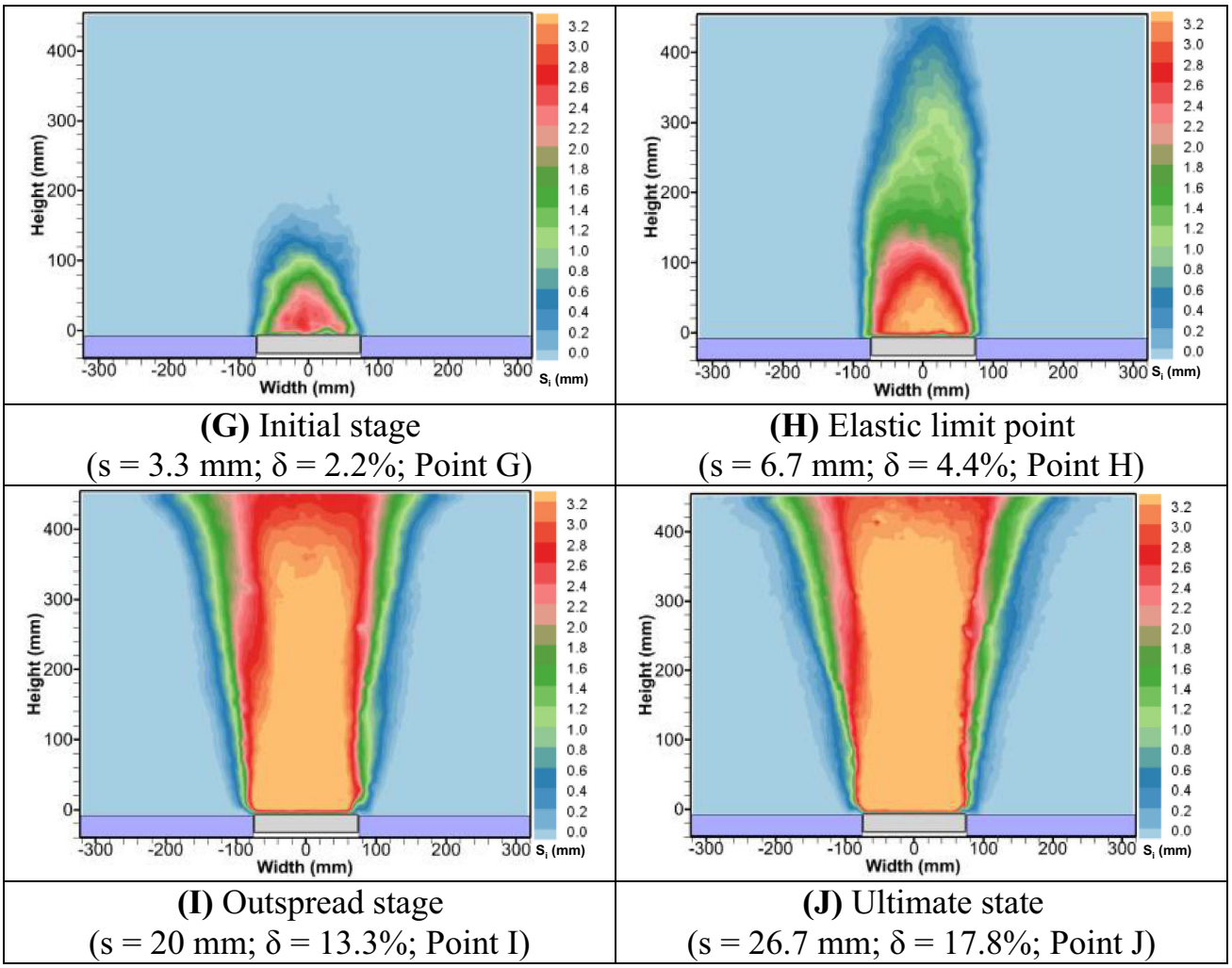

Fig. 8 Incremental displacement in typical stages in the SP-IP (Note: unit: mm; points **G** and **H** are marked in Fig. 7)

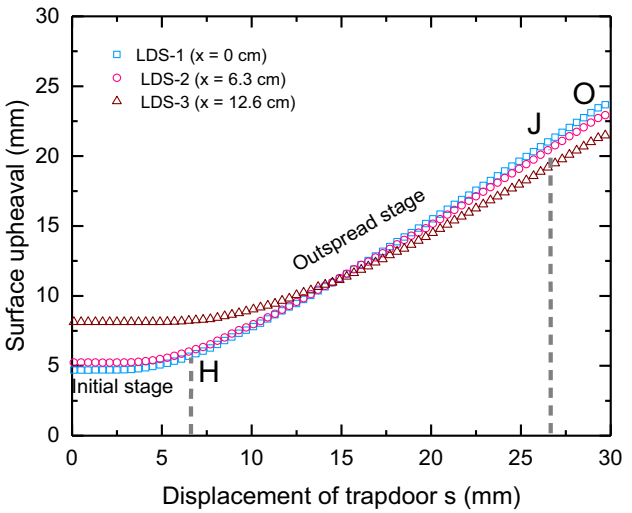

Fig. 9 Surface upheaval versus displacement in the SP-IP at *i* of 3 (Note: *x* is the distance between the LDS and the centerline of the trapdoor)

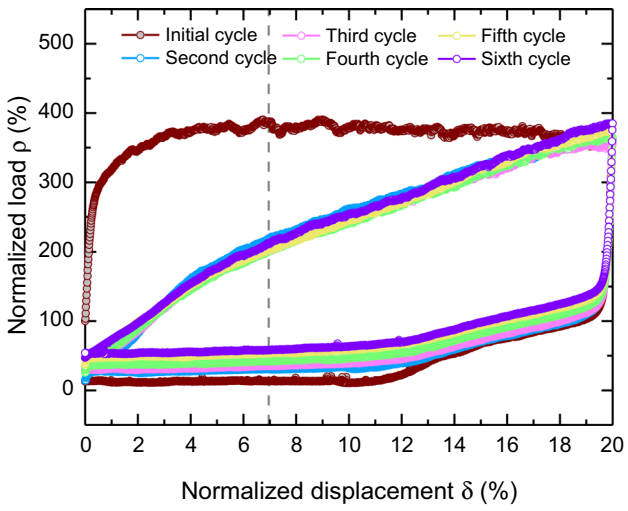

Fig. 10 Load–displacement curve in different cycles at *i* of 4

soil stress–strain hysteresis cycle under cyclic load, it is possible that the soil can adjust the dislocation between particles during multiple cycles. The energy consumed by the sliding shear and friction gradually decreased, and the viscous damping of sand particles also decreased [20, 37]. Load–displacement curve in the initial cycle is not closed as the soil is in the initial dense state exhibiting strong particle interlock. While in the subsequent cycle, as the soil becomes loose after previous upward and downward movement, the degree of particle interlock subsidesand the load–displacement curve tends to be closed.

The cumulative surface upheaval Sc was plotted against the number of cycles n in Fig. 11. It is evident that the surface upheaval appeared in the initial cycle and then decreased with the increase of n. For $i = 4$, even the surface settlement appeared. The critical embedment ratio i_{cri} was often determined when surface settlement is equal to zero. Regarding as surface deformation, the i_{cri}, where no surface settlement occurs after continuous loading and unloading, may be determined between 3 and 4 in this study. This also implies that when i is larger than i_{cri}, there will be a larger surface settlement after cycles of movement.

The stress change ratio (SCR) is defined as normalized load at a normalized displacement corresponding to the peak resistance in the IP for passive state (or ultimate load for active state) (see dotted line in Fig. 10), indicating the degree of arching effect. If SCR is equal to one, this means that no arching effect exists. The SCR versus with the number of cycles was shown in Fig. 12. For passive state, it can be seen that SCR sharply decreased after the initial cycle, which means that mobilized arching in the soil decreased substantially after the initial cycle. Then, SCR tended to be stable in the subsequent cycles. While, for active state, SCR gradually increased with the increase in the number of cycles. Similarly, the degree of active arching gradually weakened.

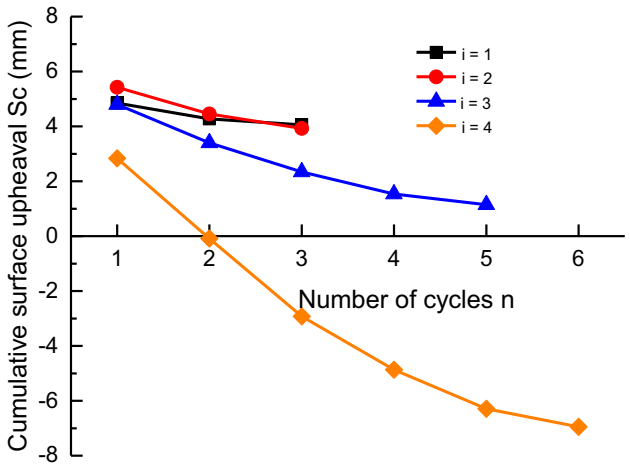

Fig. 11 Cumulative surface upheaval versus number of cycles at different embedment ratios

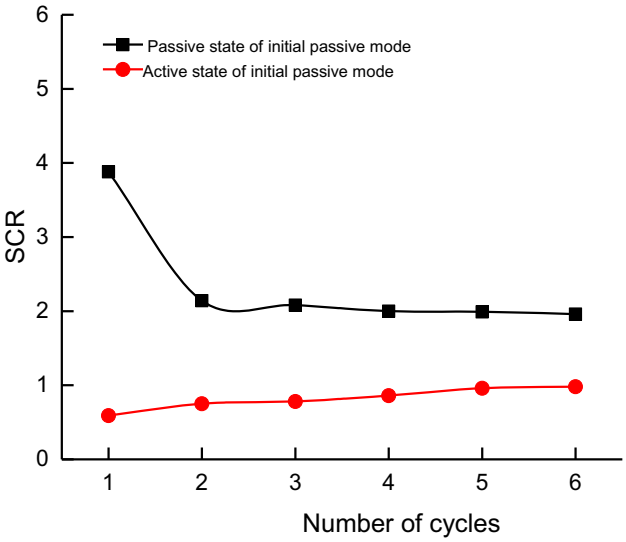

Fig. 12 Stress change ratio of the passive state and active state of initial passive mode versus number of cycles at i of 4

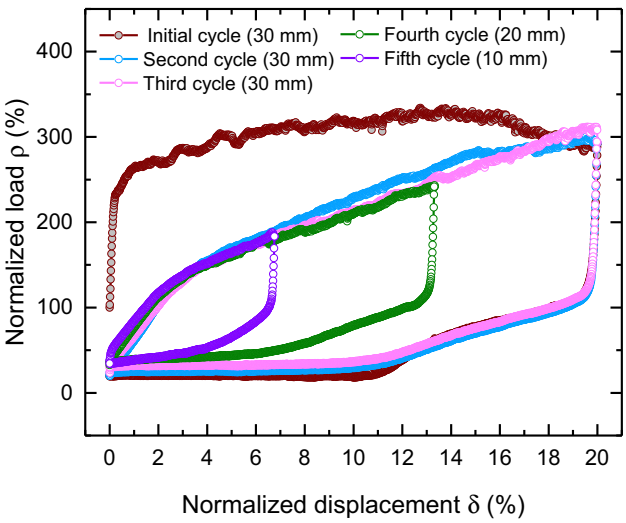

Fig. 13 Load–displacement for decreasing displacement at i of 3

2.2.4 Effect of magnitude of trapdoor displacement

When the magnitude of trapdoor displacement decreased, the load–displacement relationships in the subsequent cycles at i of 3 are presented in Fig. 13. Irrespective of the predetermined uplift displacement, it shows that ρ followed the similar path in each passive state. However, for active state, depending on the magnitude of displacement, similar paths were followed up to reach almost the same minimum load. This indicates that the degree of arching effect varies with the relative displacement.

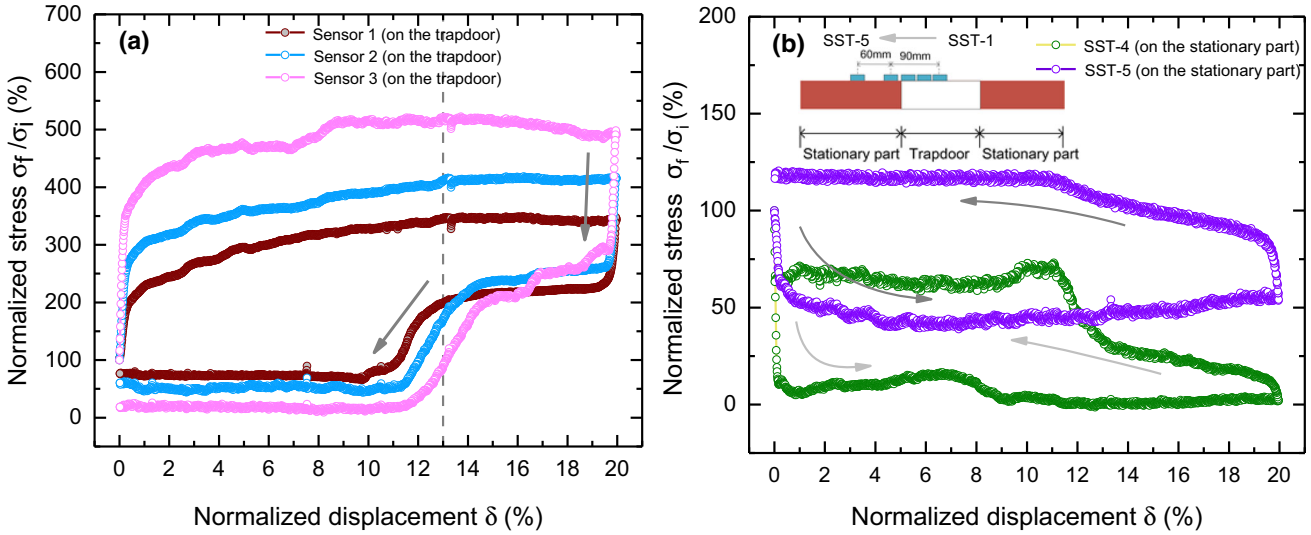

Fig. 14 Normalized stress in the initial cycle of initial passive mode at *i* of 4: **a** on the trapdoor; **b** on the stationary part

2.2.5 Stress response

Soil stress above the trapdoor were measured to investigate stress response and load transfer during alternant active and passive movements. Figure 14 shows the normalized stress (measured stress values σ_f divided by the initial values σ_i) recorded by SST-1, 2, 3 on the trapdoor and SST-4, 5 on stationary part at *i* of 4. Only the soil stress in the initial cycle was studied because the residual stress induced by particle interlock in soil body occurred and it may influence on the measurement of soil stress. The results shows that when the trapdoor was uplifted, the stresses on the trapdoor increased but not uniformly, while decreased non-uniformly on the stationary part. SST-1 (placed in the center of the trapdoor) recorded a stress increase of approximately 340%. SST-2 registered an increase of 410%, whereas the stress recorded by SST-3 (closer to the edge of the trapdoor) resulted in the increase of 490%. On the contrary, SST-4, 5 (on the stationary part) shows reductions of approximately 90% and 50%, respectively. These proves that load transfer and stress redistribution occurred; hence, the stress distribution of the overlying sand was actually non-uniform after experiencing IP. In other words, the stress displacement curve or arching state will vary with the location for soil-trapdoor interaction.

When the trapdoor reversed to move downward, accordingly, the measured stresses were reversed. Load transfer also occurred between the trapdoor and the stationary part. For SST-1, 2, 3, all decreased to be less than the initial value (i.e., 100%). On the contrary, the reading of SST-5 increased to 120%, while SST-4 only increased to 70%. These also shows the degree of arching or load transfer reduced when the sand was disturbed by a cycle of trapdoor movement. Because the granular system has

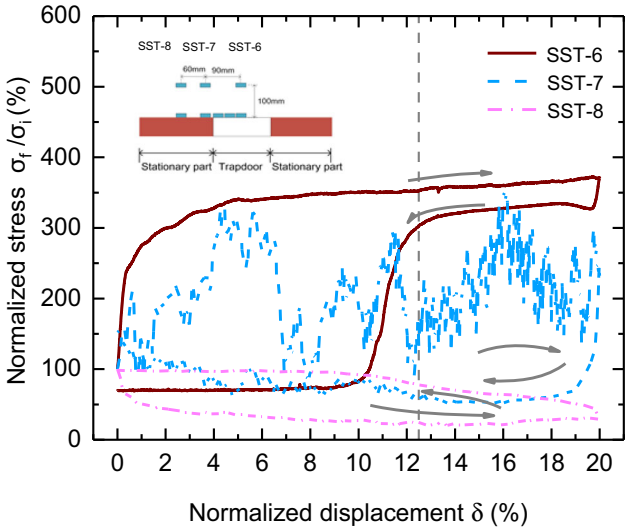

Fig. 15 Normalized stress (SST-6, 7, 8) in the initial cycle of initial passive mode at *i* of 4

experienced a significant structural transition from the initial homogeneous state to the spatially heterogeneous state.

Figure 15 shows that the normalized stress (σ_f/σ_i) recorded by SST-6, 7, 8 in the sand body during the initial cycle. In the IP, SST-6 shows a stress increasing of approximately 350%, while SST-8 shows approximate 80% reduction. Interestingly, the reading of SST-7 was out of order probably because it was located on the slip band above the trapdoor. The development of slip surface resulted in irregularly rising and falling readings of the SST. However, when the trapdoor was reversed to move downward, SST-7 was no longer located on the possible slip surface; hence, the reading of SST-7 appeared to be

functional. It is evident from SST-6 that the sharp stress reduction did not occur immediately as the load displacement curve of classical active arching, but occurred approximately at δ of 12.5% relative to the initial position, which means soil arching cannot be fully mobilized in sand immediately after initial passive disturbance.

2.3 Results of initial active mode

The initial movement direction has a significantly effect on the ground conditions (i.e., stress distribution and deformation characteristics). The load–displacement responses of initial active mode are shown in Fig. 16. Here, δ is considered to be negative. Again, the load–displacement curve was also divided into initial cycle and subsequent cycle.

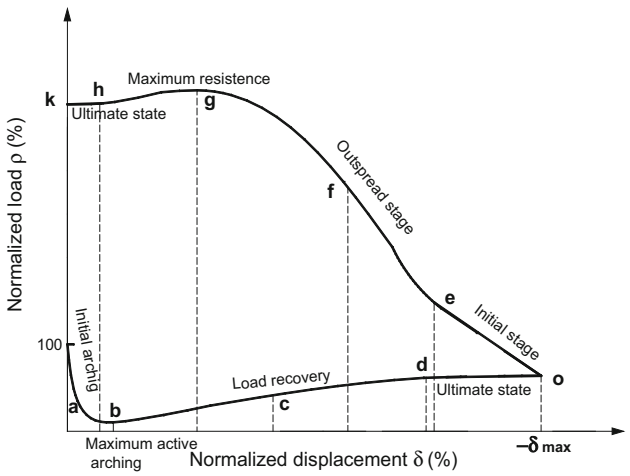

Fig. 17 Typical phases of load–displacement curve for the initial cycle of initial active mode

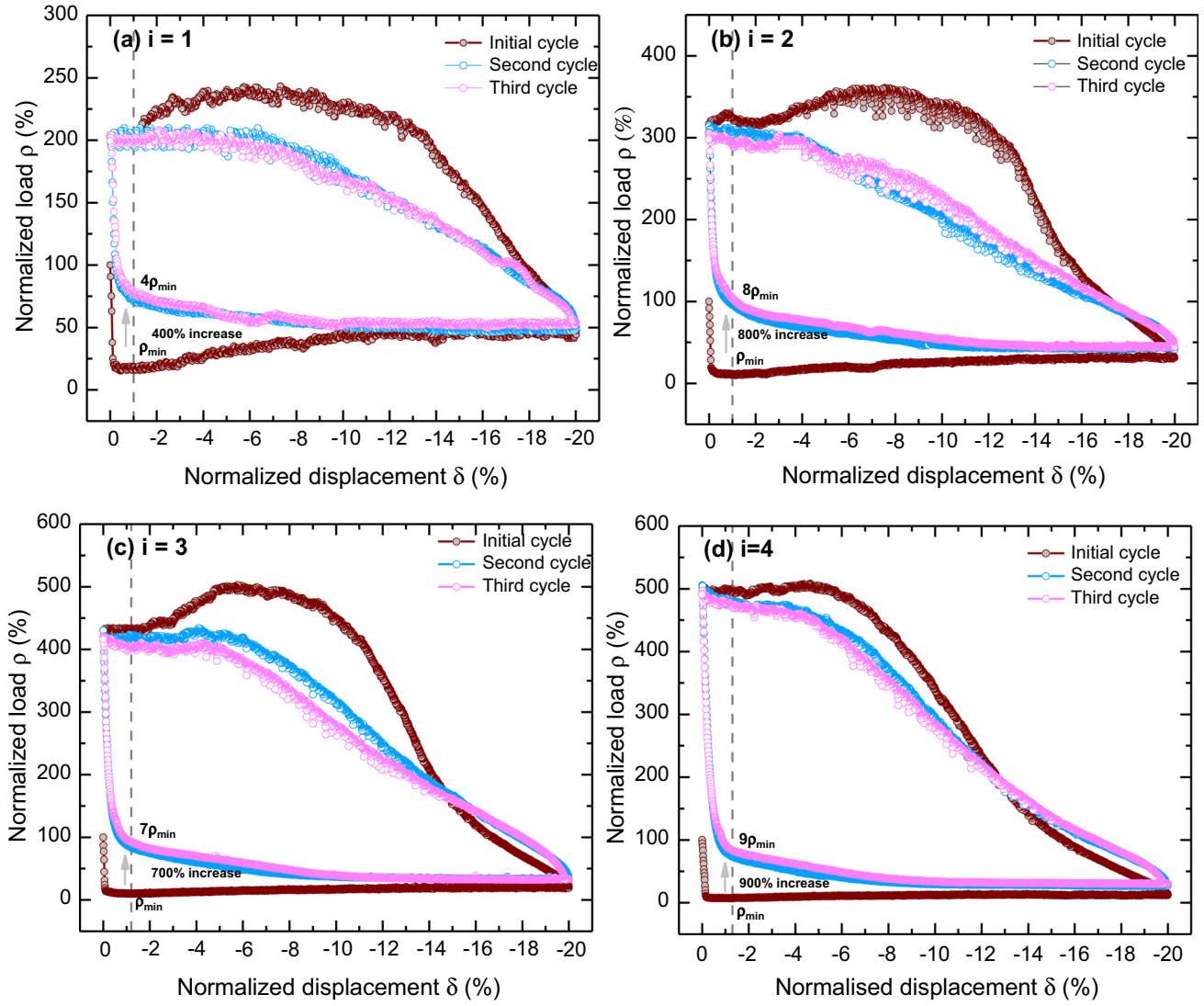

Fig. 16 Load–displacement curves for initial active mode in different embedment ratios

2.3.1 Initial cycle

Initial cycle can be divided into two specific states: initial active state (IA) and subsequent passive state (SP-IA). Several transitional phases or feature points are selected and defined in Fig. 17 to describe the development of arching. For IA, the development of soil arching or load can be described by the four-stage model [24, 53], here, feature points b and d represent maximum arching and ultimate state, respectively. Whereas, points a and c are transitional phase of arching evolution process, namely, initial arching and load recovery. For SP-IA, feature points e and g are the two break points of load displacement curve, represent the end of initial stage and maximum resistance state, respectively. Point f is transitional phase and represent outspread stage. Point h can be called as ultimate state.

Figure 18 shows S^i at selected points in typical four stages in IA. It is observed that the influence zone took on an approximately triangular shape in the initial arching stage (Fig. 18a) and maximum active arching state (Fig. 18b), then it expanded upwards and the shape changed from the initial triangular to an approximately trapezoid shape (Fig. 18c). In the ultimate state (Fig. 18d), the influence zone grew increasingly taller, taking approximate a rectangle shape.

When the trapdoor was reversed to achieve the SP-IA, the overlying sand had been disturbed by the initial active movement. As shown in Fig. 16, the load on the trapdoor firstly increased to a peak value and then decreased to an ultimate value with the uplift of the trapdoor. According to selected feature points (e, f, g and h), the load evolution of the SP-IA was divided into four typical phases in Fig. 17: initial stage (o ∼ e), outspread stage (e ∼ g), maximum resistance state (g) and ultimate state (h ∼ k).

S^i at selected points are presented in Fig. 19. A parabolic-shape influence zone was observed above the trapdoor in the initial stage (Fig. 19e). Then, the influence zone extended upwards toward the surface forming a higher parabola zone in the outspread stage (Fig. 19f). After the influence zone reached the surface, an inverted isosceles trapezoid zone was observed in both maximum resistance state (Fig. 19g) and ultimate state (Fig. 19h).

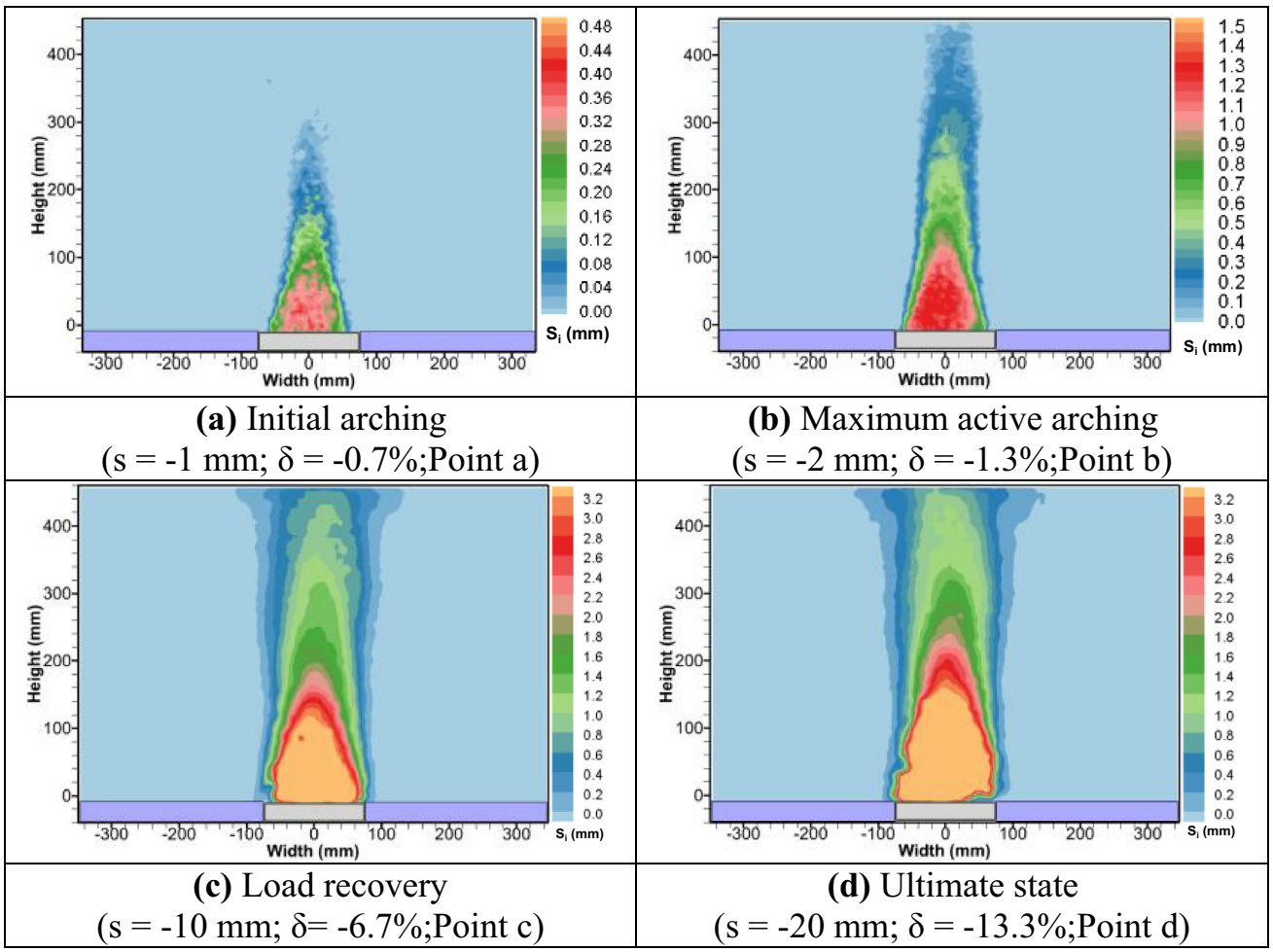

Fig. 18 Incremental displacement in typical stages in the IA (Note: unit: mm; points **a**, **b**, **c** and **d** are marked in Fig. 17)

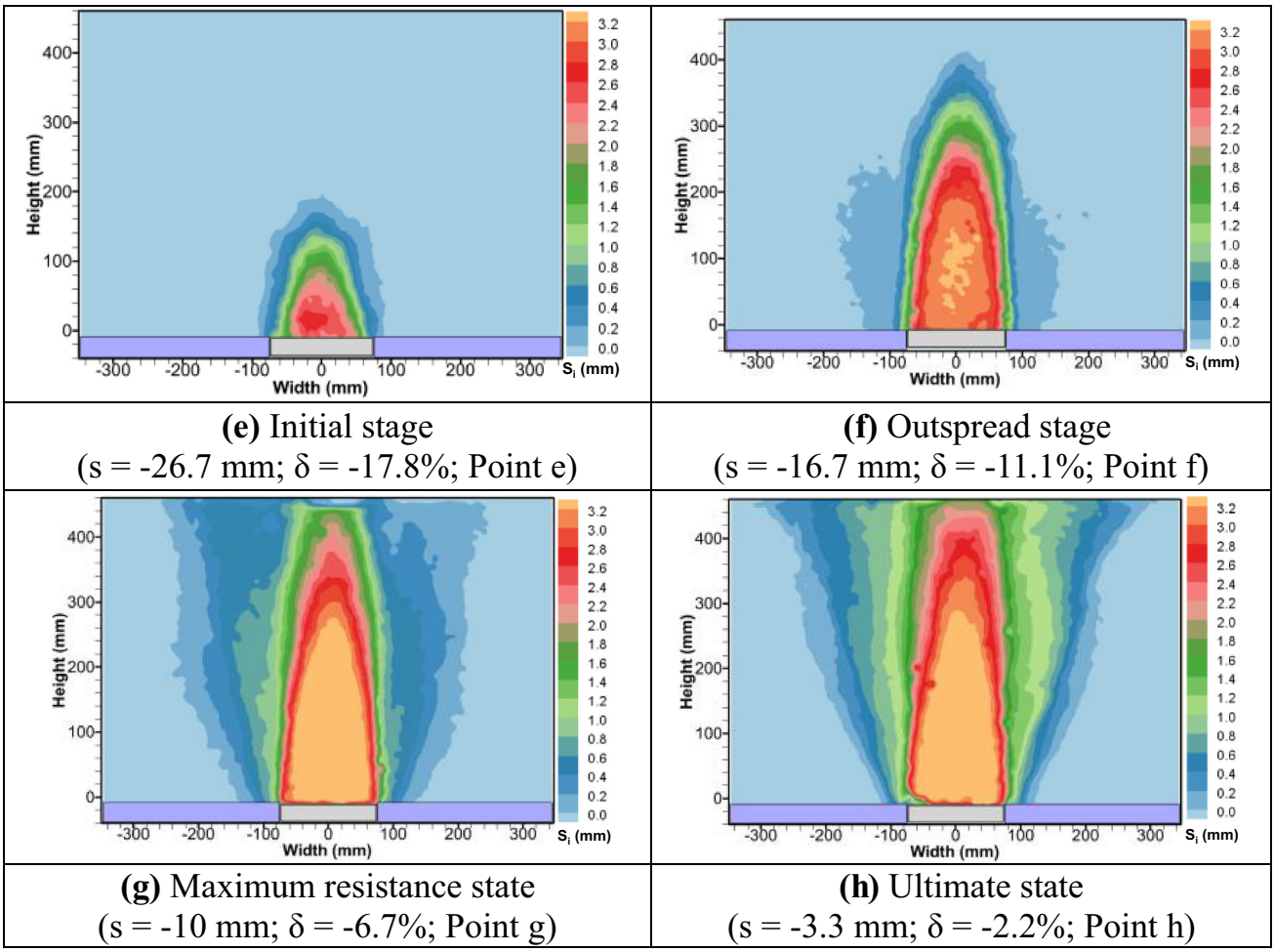

Fig. 19 Incremental displacement in typical stages in the SP-IA (Note: unit: mm; points **e**, **f**, **g** and **h** are marked in Fig. 17)

2.3.2 Subsequent cycle

When the trapdoor receded again for the subsequent active state (SA-IA), the load on the trapdoor decreased monotonically, which was similar to the SA-IP in Sect. 2.2.1. Three typical phases, including initial stage (k ∼ i), convergence stage (i ∼ m) and ultimate state (m ∼ o), are defined in Fig. 20. Here, feature points i and m represent the break point of load displacement curve and ultimate load, respectively. Whereas, points j and l are intermediate phases.

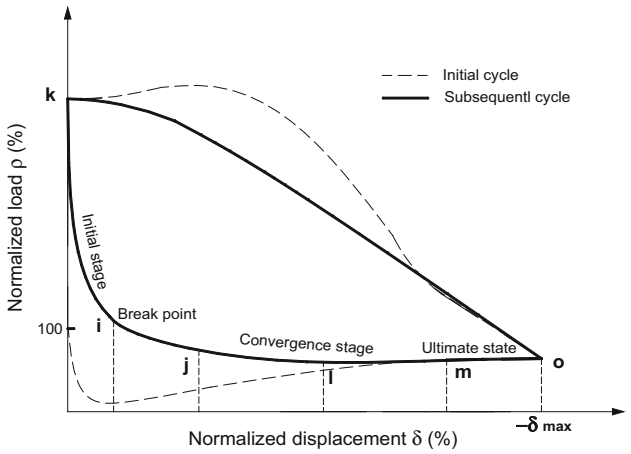

Fig. 20 Typical phases of load–displacement curve for the subsequent cycle of initial active mode

S^i at selected points are presented in Fig. 21. An inverted trapezoidal influence zone was observed in the initial stage (Fig. 21i), which was much larger than the triangular influence zone in the IA (Fig. 18b). As the trapdoor receded further, the area of influence contracted inward and downward in the convergence stage (Fig. 21j and l). A parabolic-shaped area was highlighted above the trapdoor in the ultimate state (Fig. 21m). Specifically, it was similar to the ultimate state in the IA (Fig. 18d). Due to the similar failure mechanism, the ultimate load in both two states were approximately equal. Figure 22 shows surface displacement along the centerline of the trapdoor (recorded by LDS-1) in initial cycle and SA-IA. There was cumulative upheaval S^a after a cycle of downward and

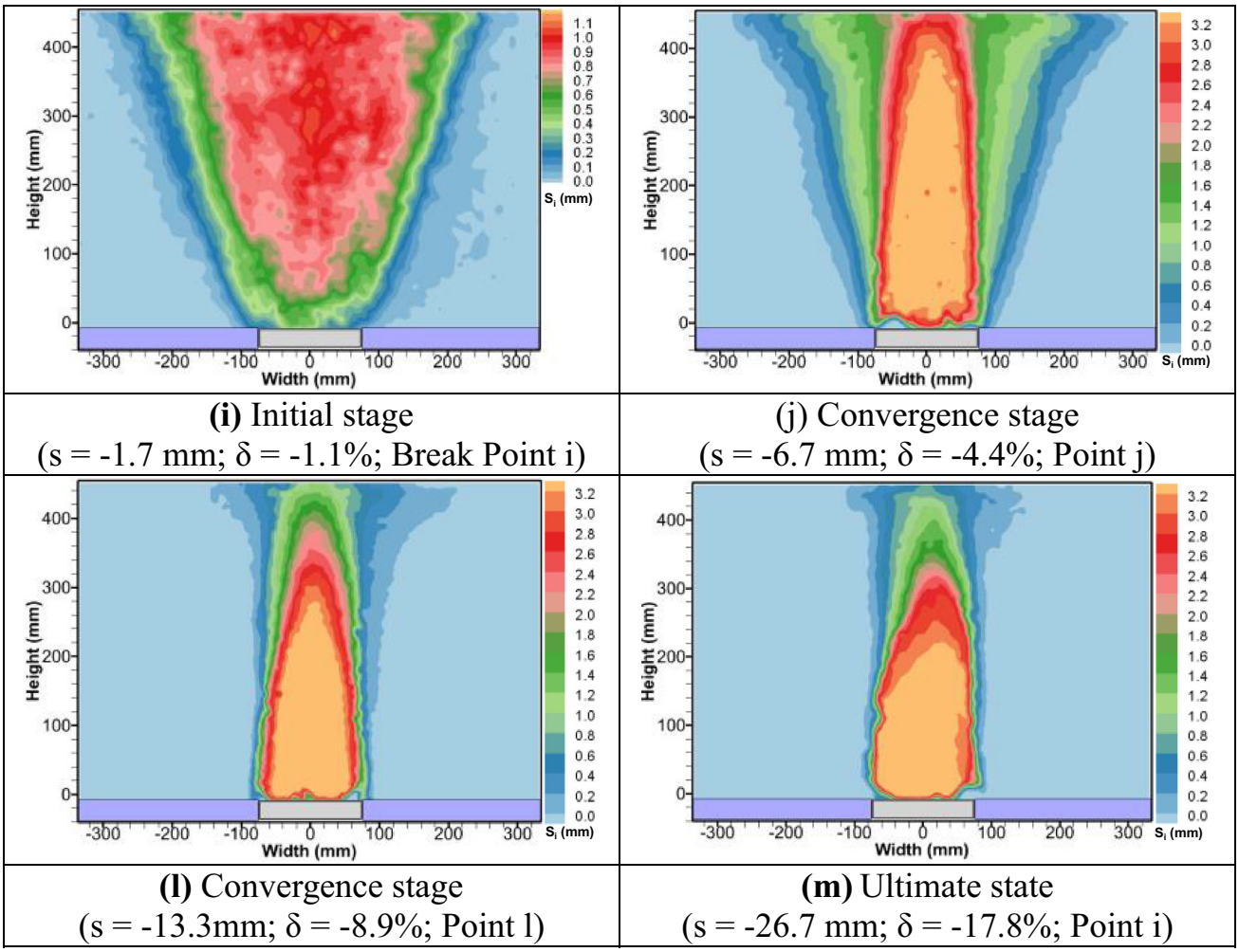

Fig. 21 Incremental displacement in typical stages in the SA-IA (Note: unit: mm; points **i, j, l** and **m** are marked in Fig. 20)

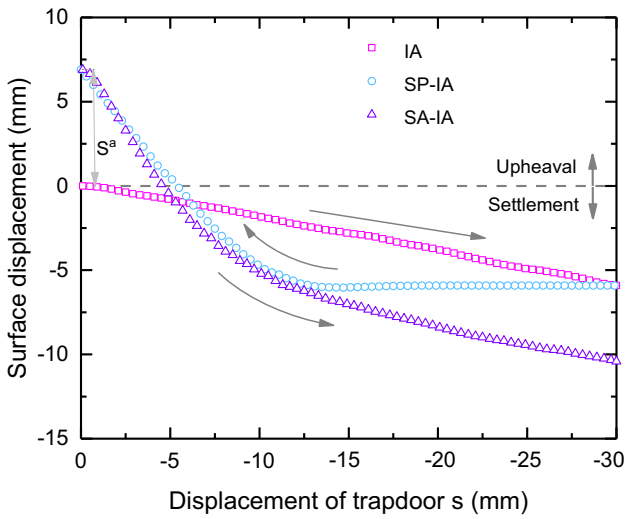

Fig. 22 Surface displacement along the centerline of the trapdoor (recorded by LDS-1) in the initial cycle (IA and SP-IA) and SA-IA of initial passive mode at *i* of 3

upward movement, which means the sand became loose after ground disturbance. Besides, it is evident that the surface settlement in SA-IA was much larger than that in IA. This implies that excessive settlement would appear in active state after alternant upward and downward movements.

The load–displacement curves of the subsequent cycles were similar to the second cycle and had coincident paths. As shown in Fig. 16, for subsequent cycles, there were no longer exhibiting minimum loads at δ_{min} corresponding to the maximum arching in IA. Meanwhile, the load increased approximately from four to nine times at δ_{min}. That is, when the overlying sand experiencing the initial cycle of movement, there will be no load recovery stage and the arching effect in SA-IA would not be fully exerted at δ_{min}.

2.3.3 Effect of moving speed of trapdoor

In Test II-4, the moving speed of trapdoor v was 2 mm/min in the first three cycles. Then, 10 and 20 mm/min

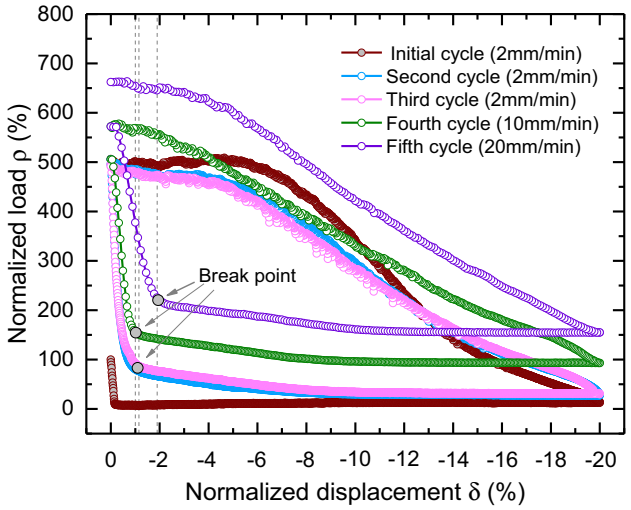

Fig. 23 Load–displacement for increasing moving speed of trapdoor at i of 4

were taken in the fourth cycle and fifth cycle, respectively. Load–displacement curves are shown in Fig. 23. The results shows that the load–displacement curve deviates from the stable paths with the increasing of v. A faster v will exacerbate the load deviation. The break point, where the curvature of the curve was the greatest, was marked in Fig. 23. For active state, the results show that with the increasing of v, loads at break point in the SA-IA increased. When the speed increased 5 times to 10 mm/min, the load increased about 1.5 times, while the load increased approximately 2 times when the speed increased 10 times to 20 mm/min. It means that the degree of load transfer significantly reduced at a higher moving speed during active state. The possible reason is that the faster speed will significantly disturb the soil structure. Consequently, the arching effect was more difficult to be mobilized. For passive state, the peak uplift resistance increased sharply with the increasing of v. This may be attributed to strain rate effect on the stress–strain behavior. Yamamuro et al.[49] found that as the v increased, the maximum principal stress ratios and the elastoplastic stiffness of sand increased. Similarly, Bransby et al. [5] observed that faster pipeline uplift displacement rates would result in both the soil uplift resistance and the distance required to mobilize peak load increasing.

2.4 Discussion on practical implications

Trapdoor tests presented the deformation behavior and load evolution, which gives a basic understanding of alternant active and passive trapdoor mechanisms and provides some implications for ground subjected to alternant disturbance. Some new findings and simply discussions are summarized as follows.

(i) If the ground has suffered from alternant active and passive disturbance, the initial stress balance of the adjacent soil in the ground can be inevitably affected, and redistribution of the in situ stresses related to the ground deformation will occur. The development of arching effect in the soil will exhibit quite different behavior compared to classical active or passive arching effect. For more comparative analysis of different active or passive states, interested readers can refer to the previous research of this subject [52].

(ii) A larger minimum load and a smaller maximum resistance on the trapdoor were observed in the subsequent movements (recall Figs. 2 and 16), which indicates the degradation of arching effect. If the underground structures suffered from upward or downward movement, load estimation based on the classical arching mechanism may significantly deviate from the actual load condition. This deviation may lead to inaccurate estimation of load or improper construction strategy, e.g., improper support pressure for tunneling, and inaccurate upheaval resistance for pipeline.

(iii) The initial mode (active or passive mode) has a significant impact on the loading-displacement curve (recall Figs. 2 and 16). In some practical cases, the true initial mode can be simply identified. For example, for a tunnel subjected to differential settlement or a subsided drainage pipeline, then, they were uplifted by the grouting technology. Certainly, this process can be considered as initial active mode. However, in some situations, it is difficult to identify the true initial mode in practice. Nevertheless, regarding previous disturbance, some phenomena can help engineers or researchers simply identify whether the ground has experienced disturbance or not. For instance, a sharp load reduction (even over 100% original self-weight) imply that previous stress transfer has been happened.

(iv) Excessive settlement of the overlaying soil may be observed when the buried infrastructures experienced upward and downward movement cycles within its service life (recall Fig. 11). In practice, when the ground with local initial elevation (e.g., grouting) or initial loss (e.g., tunneling) is subjected to unloading activities (e.g., surrounding tunnel excavation), the maximum surface settlement caused by subsequent unloading activities will increase sharply, and even much larger than that in original geostatic stress state (recall Fig. 22). Therefore, a larger support pressure and sufficient synchronous grouting are necessary for tunneling than that determined by classical earth pressure theory.

(v) Faster speed sharply disturbed the soil and affected the formation of active and passive arching (recall Fig. 23). The degree of load transfer will be significantly reduced in active state and the peak uplift resistance increased sharply in subsequent passive state with the increase in moving

speed. Hence, the effect of speed should be taken into account in load estimation in some practical engineering applications.

Overall, one of most important issues is to evaluate the vertical load on buried structure. It is expected that the visualized kinematic mechanisms and mechanical behavior will provide a fundamental basis for mathematical modeling of load on the buried structure, which provides guidance for above geotechnical applications. Therefore, the next part will give some simple and basic solution on arching load.

3 Mathematical modeling

According to the test results, when the trapdoor experienced alternating upward and downward movement, the failure mechanisms were significantly different from classical active or passive trapdoor tests. Hence, the load–displacement response was notably deviated from curve of initial active or passive test. Consequently, it is inaccurate and unsatisfactory to estimate the load based on the classical arching mechanism if previous disturbance exists. To estimate the load on the buried structures more reasonably and accurately in their entire life cycle, the alternant active and passive trapdoor problem was proposed. It is assumed to be a plan strain problem and treated as a statical analysis, without considering the effect of moving speed. The soil is cohesionless and no surface surcharge exist. Under the above assumptions, trapdoor load in the typical development states of arching was calculated by limit equilibrium method based upon the kinematic mechanisms. Normalized displacement corresponding to typical states was obtained from the tests results in this study and the literatures. Then, the simplified ground reaction curves (GRC) representing the development of arching were proposed to describe the load evolution.

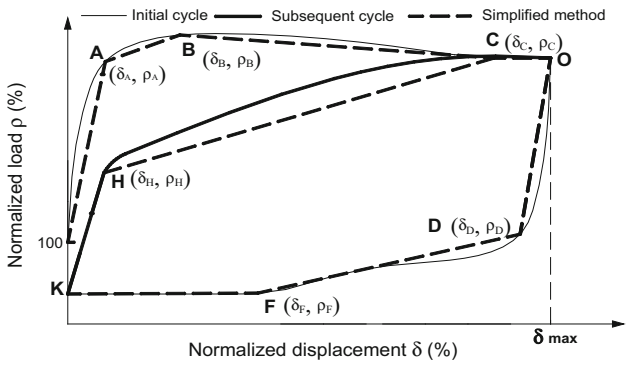

Fig. 24 Simplified GRCs of initial passive mode

3.1 GRC of initial passive mode

The GRC of initial passive mode was divided into two types: (a) initial cycle; (b) subsequent cycle. Both of them are simplified into several linear lines with several typical points including A (δ_A, ρ_A), B (δ_B, ρ_B), C (δ_C, ρ_C), D (δ_D, ρ_D), and F (δ_F, ρ_F) in the initial cycle and H (δ_H, ρ_H) in the subsequent cycle, as shown in Fig. 24. δ is related to the particle characteristic (e.g., grain size, shape), test conditions (e.g., embedment ratio, stress level and inclusion width) [53], etc. Due to the complex influencing factors, it is difficult to be determined δ by deterministic expression with perfect accuracy. Therefore, more tests and numerical simulation with different materials properties and test conditions should be performed to facilitate estimating δ in the future. Regardless, this study not emphasize on the quantitive displacement. More focus on evaluating load ρ is paid. The methods for determining ρ in several typical states are introduced as follows.

3.1.1 Initial cycle

(1) $\boldsymbol{\rho_A}$ in IP

A vertical slip mechanism was adopted for ρ_A in Fig. 25a. Based on the solutions to the uplift resistance of passive trapdoor given by Evans [18], ρ_A can be given by

$$\rho_A = \frac{P_A}{\gamma HB} = \frac{B}{2K_0 H \sin\varphi}\left(e^{2K_0\frac{H}{B}\sin\varphi} - 1\right) \quad (1)$$

where P_A is the initial uplift resistance per unit length for the trapdoor, φ is friction angle of the soil, here, it is suggested to be equal to the peak friction angle (i.e., $\varphi = \varphi_p$). K_0 is the initial lateral earth pressure coefficient, and it can be determined as

$$K_0 = \frac{\sigma_{x0}}{\sigma_{z0}} = 1 - \sin\varphi \quad (2)$$

where σ_{x0} is initial horizontal stress. σ_{z0} is initial vertical stress. Here $\sigma_{z0} = \gamma z$.

(2) $\boldsymbol{\rho_B}$ and $\boldsymbol{\rho_C}$ in IP

A simplified kinematically admissible mechanism (Fig. 25b) was adopted for obtaining solutions of peak uplift resistance ρ_B and ultimate uplift resistance ρ_C. In this case, the uplift resistance is equal to the lifted soil weight plus the resultant vertical force on the slip planes, which arises from both the shear and the normal stresses. Then, the uplift resistance is simply the weight of the lifted soil [11, 48]. If not consider the dilatancy effect, the inclination angles of slip surface θ (measured between the vertical direction and the slip surface) were approximately equal to φ [48], which will give a maximum

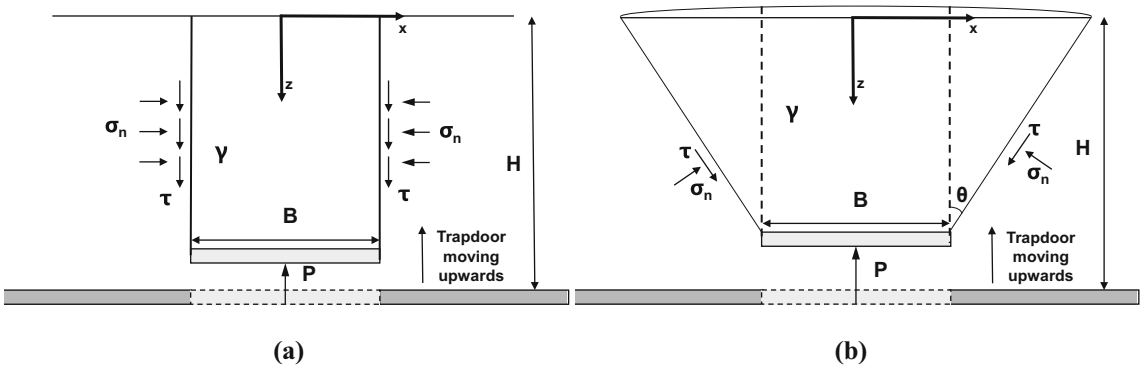

Fig. 25 Schematic of mechanism for IP: **a** vertical slip mechanism in the initial passive stage for ρ_A; **b** inclined slip mechanism in maximum passive arching state and ultimate state for ρ_B and ρ_C

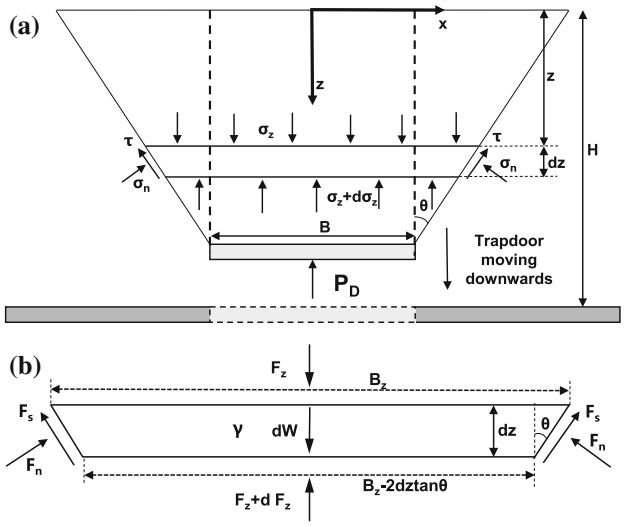

Fig. 26 Schematic of load estimation for ρ_D in SA-IP: **a** assumed slip surface and a typical soil element; **b** Forces acting on the soil element

solution. In the maximum passive arching state and ultimate state, the uplift resistance (i.e., peak uplift resistance P_B and ultimate uplift resistance P_C) can be acquired when φ is equal to φ_p and φ_{cri}, respectively. Hence, ρ_B and ρ_C can be given by

$$\rho_B = \frac{P_B}{\gamma HB} = 1 + \frac{H}{B}\tan\varphi_p \tag{3}$$

$$\rho_C = \frac{P_C}{\gamma HB} = 1 + \frac{H}{B}\tan\varphi_{cri} \tag{4}$$

(3) $\boldsymbol{\rho_D}$ and $\boldsymbol{\rho_F}$ in SA-IP

Similar as ρ_C, an inverted trapezoidal shape of failure mechanism was adopted for ρ_D in Fig. 26. Differently, the failure wedge is subject to upward friction along the boundary. The following derivation of ρ_D is based on this failure mechanism and assumption.

In the mathematical modeling part, the lateral earth pressure coefficient K is the key parameter in obtaining the aimed ratio. Generally, K is defined as the ratio between the horizontal stress (σ_x) and the vertical stress (σ_z) and then it is given as

$$K = \frac{\sigma_x}{\sigma_z} \tag{5}$$

For trapdoor problem, K is not easy to be determined as stress transfer and principle stress rotation with trapdoor movement. Different researchers have proposed different methods to determine K values in both active and passive states [1, 8, 18, 44]. However, most of the method only provide a constant value of K. In this part, Different from previous methods, considering K may change as the trapdoor moving, each ratio ρ is related to the K at that stage. Namely, K is considered to be a parameter related to the mobilization degree of arching effect.

The vertical stress σ_z during the development of arching can be given as

$$\sigma_z = \rho\gamma z \tag{6}$$

where ρ is arching ratio (i.e., normalize load).

For deriving ρ_D in this study, the horizontal stress (σ_x) during trapdoor tests was considered to remain fairly constant as recent study [18, 44], then, it was taken as the initial at rest. Considering that $\sigma_x = \sigma_{x0}$, substituting Eqs. (2) and (6) into Eq. (5) gives

$$K = \frac{K_0}{\rho} = \frac{1-\sin\varphi}{\rho} \tag{7}$$

Therefore, K is expressed in terms of ρ. For active state, $\rho < 1$, then $K > K_0$. This is consistent with previous estimation about K value, e.g., $K = 1 > K_0$ adopted by Terzaghi [44] and Vardoulakis et al. [45], $K = 1.2 > K_0$ adopted by Evans [18]. Whereas, for

passive state, $\rho > 1$, then $K < K_0$. This is in agreement with the K adopted by Evans [18], where $K = (1 - \sin\varphi) / (1 + \sin\varphi) < 1 - \sin\varphi = K_0$.

Substituting ρ_D in Eq. (7) gives K_D in Eq. (8).

$$K_D = \frac{K_0}{\rho_D} = \frac{1-\sin\varphi}{\rho_D} \tag{8}$$

For a homogeneous sand, the normal stress (σ_n) on an inclined section at any depth z below the surface can be expressed in terms of the vertical stress (σ_z) and horizontal stress (σ_x) as the principal stresses [40]. Then, the normal stress (σ_n) can be given from Eq. (9).

$$\sigma_n = \frac{(1+K) - (1-K)\cos 2\theta}{2}\sigma_z \tag{9}$$

If defining another coefficient K_h as the ratio of normal stress (σ_n) to vertical stress (σ_z), then K_h can be given as

$$K_h = \frac{(1+K_D) - (1-K_D)\cos 2\theta}{2} \tag{10}$$

On the basis of obtaining K_D and K_h, the analytical solution to ρ_D can be given by

$$\rho_D = \frac{P_D}{\gamma HB} = \frac{B}{2\tan\theta H\left(2 - \frac{K_h(\tan\theta+\tan\varphi)}{\tan\theta}\right)\left[\left(\frac{B+2H\tan\theta}{B}\right)^{2-\frac{K_h(\tan\theta+\tan\varphi)}{\tan\theta}} - 1\right]} \tag{11}$$

where P_D is the load at point D, θ was believed to be equal to ψ [14, 16]. The detailed derivation can be found in "Appendix".

For ρ_F, it can be considered to be the ultimate load in SA-IP. It is observed that there was a rectangular influence area above the trapdoor in the ultimate state (Fig. 5K), which was similar to the ultimate state of IA (Fig. 18d). Following the arching load solution by Terzaghi [44], ρ_F can be obtained based on a vertical slip mechanism in Fig. 27 [18, 44].

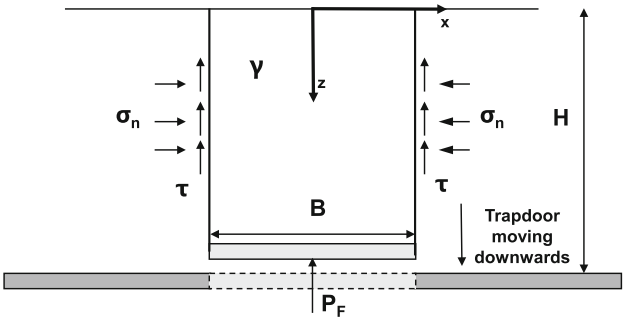

Fig. 27 Schematic of mechanism for the ultimate state of SA-IP

$$\rho_F = \frac{P_F}{\gamma HB} = \frac{B}{2KH\tan\varphi}\left(1 - e^{-2K\tan\varphi\frac{H}{B}}\right) \tag{12}$$

where P_F is the ultimate load in the SA-IP. Here, φ is suggested to be equal to φ_{cri}. Since the failure mechanism in ultimate state of SA-IP is similar to that of ultimate state of IA, K is recommended to be 1.0 for ultimate state as suggested by Terzaghi [44].

3.1.2 Subsequent cycle

(4) $\boldsymbol{\rho_H}$ in SP-IP

The load above the trapdoor increased linearly with the increase in uplift displacement until the influence zone reached the ground surface, exhibiting a vertical slip mechanism. Then ρ_H can be obtained in Eq. (13) by this simple failure mechanism.

$$\rho_H = \frac{P_H}{\gamma HB} = \frac{B}{2K_H H\sin\varphi}\left(e^{2K_H\frac{H}{B}\sin\varphi} - 1\right) \tag{13}$$

where K_H is the earth pressure coefficient at point H. Here, the peak friction angle φ_p is adopted for calculation. According to Eq. (9), K_H is related to ρ_H and it can be acquired from Eq. (14).

$$K_H = \frac{K_0}{\rho_H} = \frac{1-\sin\varphi}{\rho_H} \tag{14}$$

Substituting Eq. (14) in (13), then ρ_G can be given by Eq. (15).

$$\rho_H = \frac{2(1-\sin\varphi)\sin\varphi\frac{H}{B}}{\ln\left(1+2(1-\sin\varphi)\sin\varphi\frac{H}{B}\right)} \tag{15}$$

where P_H is load on the trapdoor at point H (see Fig. 24).

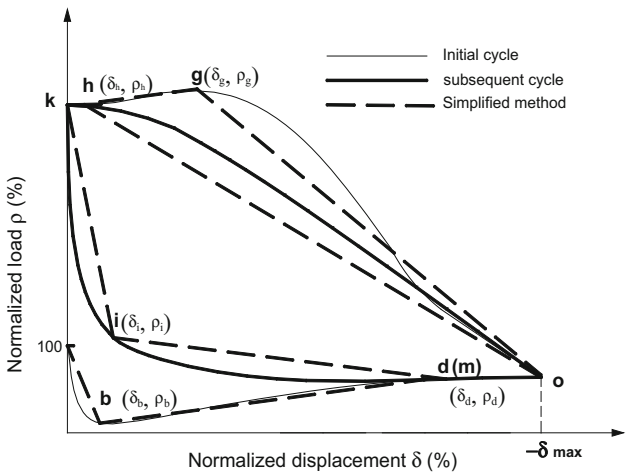

Fig. 28 Simplified GRCs of initial active mode

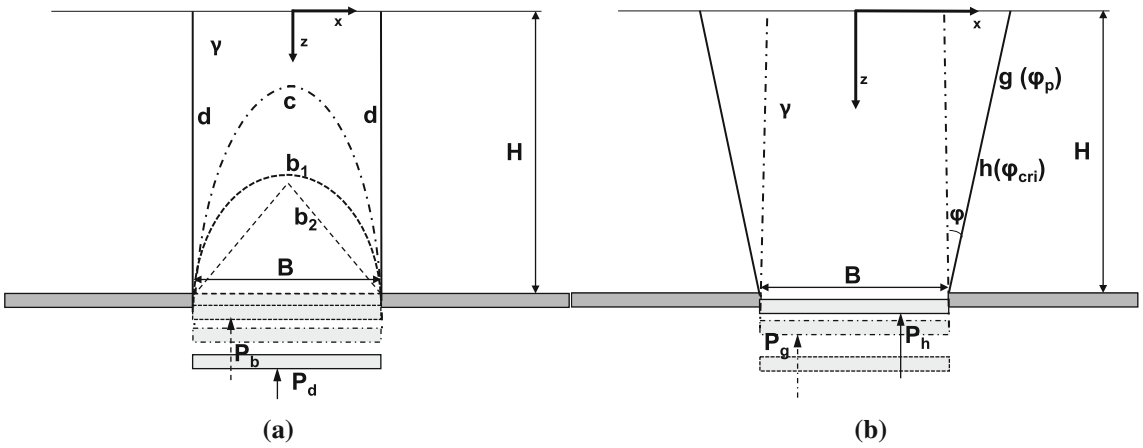

Fig. 29 Schematic of arching mechanisms: **a** for ρ_b in IA; **b** for ρ_f and ρ_g in SP-IA

3.2 GRC of initial active mode

Similarly, the GRC of initial active mode, including (a) initial cycle and (b) subsequent cycle, are simplified into several linear lines with five typical points including b (δ_b, ρ_b), d (δ_d, ρ_d), g (δ_g, ρ_g), h (δ_h, ρ_h) in the initial cycle and i (δ_i, ρ_i) in the subsequent cycle, as shown in Fig. 28.

3.2.1 Initial cycle

(1) $\boldsymbol{\rho_b}$ and $\boldsymbol{\rho_d}$ in IA

As the trapdoor receded, three distinct failure phase mechanisms, shifting from curve b to curve c and curve d, can be illustrated in Fig. 29a. Considering curve b_1 for parabolic arch or b_2 for triangular arch in Fig. 29a, a minimum load on trapdoor can be achieved for the maximum soil arching was mobilized.

Following these different failure mechanisms, a simple solution of ρ_b were given by Iglesia et al. [25]. For parabolic shape,

$$\rho_{b_1} = \frac{P_{b_1}}{\gamma HB} = \frac{B}{H}\left(\frac{K_E}{2\cot\varphi + \frac{BK_E}{H}} + \frac{\cot\varphi}{6}\right) \tag{16a}$$

or for triangular shape,

$$\rho_{b_2} = \frac{P_{b_2}}{\gamma HB} = \frac{B}{H}\left(\frac{K_E}{4\cot\varphi + \frac{BK_E}{H}} + \frac{\cot\varphi}{4}\right) \tag{16b}$$

where P_b is load in the maximum active arching state, $K_E = (1 - \sin^2\varphi)/(1 + \sin^2\varphi)$. Here, the very small displacement of the trapdoor means a minor strain level, suggesting that the peak friction angle is more reasonable (i.e., $\varphi = \varphi_p$ in Eq. (16)) [12]. Detailed derivation can be referred to Iglesia et al. [25]. A triangular arch configuration deformation pattern was observed in this experiment and then Eq. (16b) was adopted for in ρ_b in this study.

In the ultimate state, curve d illustrated vertical failure mechanism. According to the basic solution of Terzaghi [44], ρ_d can be given as

$$\rho_d = \frac{P_d}{\gamma HB} = \frac{B}{2KH\tan\varphi}\left(1 - e^{-2K\tan\varphi\frac{H}{B}}\right) \tag{17}$$

where P_d is load in the ultimate state. Here, the considerable deformation in the ultimate state makes it seem fairly intuitive to accept that the shear strength of the material corresponded to the critical friction (i.e., $\varphi = \varphi_{cri}$ in Eq. (17)) [12]. K is recommended to be 1.0 as suggested by Terzaghi [44] and discussed by Chevalier and Villard [12].

(2) $\boldsymbol{\rho_g}$ and $\boldsymbol{\rho_h}$ in SP-IA

The inclined slip kinematic mechanism was adopted in Fig. 29b. The inclination angle of slip surface θ was considered to be equal to φ. It is believed that the peak friction angle was mobilized (i.e., $\varphi = \varphi_p$) in the maximum resistance state while the critical friction angle was mobilized (i.e., $\varphi = \varphi_{cri}$) in the ultimate state. Then, ρ_g and ρ_h can be simply given by

$$\rho_g = \frac{P_g}{\gamma HB} = 1 + \frac{H}{B}\tan\varphi_p \tag{18}$$

$$\rho_h = \frac{P_h}{\gamma HB} = 1 + \frac{H}{B}\tan\varphi_{cri} \tag{19}$$

where P_g and P_h is the maximum and ultimate uplift resistances. Specially, ρ_g and ρ_h are considered to be approximately equal to ρ_B and ρ_C.

3.2.2 Subsequent cycle

(3) $\boldsymbol{\rho_i}$ in SA-IA

The evolution of the failure zone observed in the

Table 2 Comparison of measured load ratios ρ with calculated ones at flag points

Mode	State	Index	$i = 1$		$i = 2$		$i = 3$		$i = 4$	
			M	C	M	C	M	C	M	C
Initial passive mode	IP	ρ_A	145	123	195	154	228	196	260	252
		ρ_B	184	202	264	304	328	406	375	508
		ρ_C	162	191	220	283	295	375	352	466
	SA-IP	ρ_D	92	100	100	112	112	127	125	142
		ρ_F	35	42	27	24	19	17	12	13
	SP-IP	ρ_H	105	119	120	137	142	153	166	169
Initial active mode	IA	ρ_b	15	32	11	16	9	11	6	8
		ρ_d	44	42	32	24	20	17	13	13
	SP-IA	ρ_g	240	202	352	304	490	406	505	508
		ρ_h	202	191	301	283	415	375	495	466
	SA-IA	ρ_i	80	100	100	112	105	127	95	142

M: measured value, C: calculated value, unit: %

initial stage in SA-IA (Fig. 21i) was similar to the initial stage in SA-IP (Fig. 5D), that is, an inverted trapezoidal shape of failure mechanism with the failure wedge subject to upward friction along the boundary. Therefore, inclined mechanism in Fig. 26 can be also adopted for ρ_i and then it can be similarly given by

$$\rho_i = \rho_D. \tag{20}$$

3.3 Verification and discussion

Before verifying the effectiveness of the proposed simplified method, dilation angle ψ firstly needed to be determined at test condition. Due to the relatively low stress level in 1 g experiment, ψ is difficult to be obtained by the triaxial tests. Here, ψ was determined by empirical equation proposed by Bolton [4] in Eq. (21).

$$\psi = 5/b[D_r(Q - \ln p) - R] \tag{21}$$

where p is stress level (kPa). b is the coefficient related to particle characteristics of soil. Q and R can be obtained from triaxial tests. Based on the ψ obtained from the triaxial tests at confining stress of 30 kPa, 50 kPa and 70 kPa, the fitting relationship between the ψ and p can be obtained. Then, for different buried depths, ψ can be determined.

The measured values and the calculated ones in typical points were compared in Table 2. Overall, most of the calculated results were in good agreement with the measured values. A few points slightly deviate from the measured values. This may be caused by the following reasons. (i) The experimental error involved with load measurements in trapdoor experiments, e.g., friction at the trapdoor edges and fixed side walls, mobilized friction between the backfill and transparent container. (ii) Simplification of load calculation model, e.g., shape of failure block, assumption on limit state, inaccurate K value, etc.

Specifically, ρ_A are slightly smaller than the measured ones. This may be because that the failure block may have slightly extended from the vertical slip mechanism to the inclined slip mechanism. The trapdoor should carry more load. For ρ_B and ρ_C, the solutions give the maximum resistance. Therefore, the calculated values are slightly larger than the measured ones. These solutions may be improved by upper bound limit analysis and considering non-associative Coulomb soil [41], which expect to give a smaller upper bound. ρ_D, ρ_F, and ρ_H are agreed with the measured ones, indicating that Eqs. (11), (12), and (15) are reasonable. For initial active state, Iglesia's solution, i.e., ρ_b, provides a large prediction, especially for shallow condition. Terzaghi's method, i.e., ρ_d, gives a consistent result. Solution of ρ_g and ρ_h always give a slightly low prediction. One of the most possible reasons is the experimental error involved friction at the trapdoor edges and fixed side walls. Whereas, solution of ρ_i is slightly larger than the measured value.

Based on the kinematic mechanisms, a rapid and effective estimation of the vertical load on the trapdoor was provided by mathematical modeling. Compared to the classic solution on arching load, the most notable improvement of this method is that the disturbed state of backfill can be considered in the estimation of vertical load on structures. Instead of focusing on the load at one point or a specific state, e.g., ultimate state with vertical failure mechanism by Terzaghi [44], load evolution with increasing mobilized displacement can be well described, which provides a new and more accurate method for the estimation of the life-cycle load on underground structures. For engineering application, if an initial ground loss or

elevation has not been experienced before estimating the vertical load, the initial cycle of the simplified GRC can be adopted. On the other hand, the second cycle of the simplified GRC should be adopted if the overlaying soil of underground structure is not in the initial geostress state.

4 Conclusions

The mechanical behavior and failure mechanism of sand body subjected to an alternant active and passive trapdoor have been studied by experimental investigation. Based on the kinematic mechanism of backfills, simplified ground reaction curves have been proposed for load estimation. The main conclusions are summarized as follows:

(a) The initial disturbance has a significant influence on the evolution of trapdoor load. Considering different trapdoor movement paths, four typical load–displacement curves at different embedment ratios were presented and described by stages with flag values to reveal the load evolution. Compared to classical active or passive trapdoor tests, a larger minimum load and a smaller maximum resistance on the trapdoor was observed during subsequent movements. Prediction trapdoor load based on classical arching mechanism could significantly deviate from the real load if the soil suffered from continuous disturbance.

(b) The initial cycle and subsequent cycle of observed load displacement curve have significantly different characteristics, whether initial active or passive mode. The subsequent cycle, though significantly deviates from that in the initial cycle, follows an almost coincident load–displacement path. Load–displacement curve in initial cycle is not closed. While in the subsequent cycle, it tends to be closed. Essentially, these characteristics dependent on density change of sand. After the initial cycle, soil arching substantially degenerates.

(c) Faster movement of the trapdoor will obviously disturb the structure of granular system and make the arching more difficult to form. As a result, with the increase in the moving speed of the trapdoor, the degree of arching effect decreases and the load–displacement curve deviates from the stable paths of the subsequent cycle.

(d) Lateral earth pressure coefficient K is one of the key parameters to determine each typical arching ratio ρ in simplified ground reaction curves. Some constant K values are adopted for ρ in the ultimate state or specific states, whereas, in the transitional state, K is considered to be a parameter related to the stress state and development of arching. The good correction between analytical solutions and test results indicates that the K value is reasonable.

(e) Two simplified GRCs representing the progressive development of arching, described by several typical states, were proposed to facilitate the application of the arching effect considering the initial disturbance in engineering practice. The guidelines for determining the required parameters were provided by limit equilibrium method based on the identified kinematic characteristic and failure mechanism. The simplified GRCs were well verified by the results from this study.

Appendix

Figure 26a shows a vertical section of the homogeneous soil mass. The slip plane inclined at an angle θ to the vertical. A soil element of thickness dz at depth z below the ground level is considered in Fig. 26b.

The self-weight (dW) of the element is obtained as:

$$dW = \gamma B_z dz = 2\gamma\left[\frac{B}{2} + (H - z)\tan\theta\right]dz \tag{22}$$

Force acting on the top of the strip (F_z) is obtained as:

$$F_z = \sigma_z B_z = 2\sigma_z\left[\frac{B}{2} + (H - z)\tan\theta\right] \tag{23}$$

Force acting on the bottom of the strip ($F_z + dF_z$) is obtained as:

$$F_z + dF_z = 2(\sigma_z + d\sigma_z)\left[\frac{B}{2} + (H - z - dz)\tan\theta\right] \tag{24}$$

The shear force (F_s) on the slip planes is given as:

$$F_s = K_h\sigma_z \tan\varphi dz \sec\theta \tag{25}$$

The force (F_n) due to normal stress (σ_n) is given as:

$$F_n = K_h\sigma_z dz \sec\theta \tag{26}$$

Since the soil mass must be in equilibrium, the vertical force balance equation can be written as:

$$F_z + dF_z + 2F_n\sin\theta + 2F_s\cos\theta - dW - F_z = 0 \tag{27}$$

Substituting Eqs. (22)–(26) in Eq. (27) provides:

$$\frac{d\sigma_z}{dz} + \frac{2(K_h\tan\theta + K_h\tan\varphi - \tan\theta)}{B + 2H\tan\theta - 2z\tan\theta}\sigma_z = \gamma \tag{28}$$

Equation (28) is a first order linear differential equation, which on solving gives:

$$\sigma_z = \left[\frac{\gamma(B+2H\tan\theta-2z\tan\theta)^{2-\frac{K_h(\tan\theta+\tan\varphi)}{\tan\theta}}}{-2\tan\theta\left(2-\frac{K_h(\tan\theta+\tan\varphi)}{\tan\theta}\right)}+C\right] \left((B+2H\tan\theta-2z\tan\theta)^{-1+\frac{K_h(\tan\theta+\tan\varphi)}{\tan\theta}}\right) \quad (29)$$

where C is a constant of integration, which can be determined by the boundary condition as $\sigma_z|_{z=0} = 0$.

Thus,

$$C = \frac{\gamma(B+2H\tan\theta)^{2-\frac{K_h(\tan\theta+\tan\varphi)}{\tan\theta}}}{2\tan\theta\left(2-\frac{K_h(\tan\theta+\tan\varphi)}{\tan\theta}\right)} \quad (30)$$

Hence, the vertical stress at a depth H below the ground level becomes

$$\sigma_z|_{z=H} = \frac{\gamma B}{2\tan\theta\left(2-\frac{K_h(\tan\theta+\tan\varphi)}{\tan\theta}\right)} \left[\left(\frac{B+2H\tan\theta}{B}\right)^{2-\frac{K_h(\tan\theta+\tan\varphi)}{\tan\theta}}-1\right] \quad (31)$$

Then ρ_D can be given as

$$\rho_D = \frac{\sigma_z|_{z=H}}{\gamma H}. \quad (32)$$

Acknowledgements This study was supported by Natural Science Foundation of China (Grant Nos. 51978523 and 51778485), and these financial supports are greatly appreciated.

References

1. Aqoub K, Mohamed M, Sheehan T (2018) Analysis of sequential active and passive arching in granular soils. Int J Geotech Eng 15(5):598–607. https://doi.org/10.1080/19386362.2018.1473195
2. Badakhshan E, Noorzad A, Bouazza A, Dafalias YF, Zameni S, King L (2020) Load recovery mechanism of arching within piled embankments using discrete element method and small scale tests. Powder Technol 359:59–75
3. Bi ZQ, Gong QM, Guo PJ, Cheng Q (2020) Experimental study of the evolution of soil arching effect under cyclic loading based on trapdoor test and particle image velocimetry. Can Geotech J. https://doi.org/10.1139/cgj-2019-0205
4. Bolton MD (1987) The strength and dilatancy of sands. Discuss Geotech 37(1):219–226
5. Bransby MF, Ireland J (2009) Rate effects during pipeline upheaval buckling in sand. Geotech Eng 162(5):247–256
6. Britton EJ, Naughton PJ (2011) The arching phenomena observed in experimental trap door model tests. In: Geo-frontier (ASCE), pp 788–797
7. Chen RP, Lin XT, Wu HN (2019) An analytical model to predict the limit support pressure on a deep shield tunnel face. Comput Geotech 115:103174
8. Chen RP, Tang LJ, Yin XS, Chen YM, Bian XC (2015) An improved 3D wedge-prism model for the face stability analysis of the shield tunnel in cohesionless soils. Acta Geotech 10(5):683–692
9. Chen Z, Tho KK, Leung CF, Chow YK (2013) Influence of overburden pressure and soil rigidity on uplift behavior of square plate anchor in uniform clay. Comput Geotech 52:71–81
10. Cheuk CY, Take WA, Bolton MD, Oliveira JRMS (2007) Soil restraint on buckling oil and gas pipelines buried in lumpy clay fill. Eng Struct 29(6):973–982
11. Cheuk CY, White DJ, Bolton MD (2008) Uplift mechanisms of pipes buried in sand. J Geotech Geoenviron Eng 134(2):154–163
12. Chevalier B, Combe G, Villard P (2012) Experimental and discrete element modeling studies of the trapdoor problem: influence of the macro-mechanical frictional parameters. Acta Geotech 7(1):15–39
13. Costa YD, Zornberg JG (2020) Active and passive arching stresses outside a deep trapdoor. Acta Geotech 15:3211–3227. https://doi.org/10.1007/s11440-020-00969-x
14. Costa YD, Zornberg JG, Bueno BS (2009) Failure mechanisms in sand over a deep active trapdoor. J Geotech Geoenviron Eng 135(11):1741–1753
15. Dai N, Shan Y, Fu LL, Ye WT, Guo PJ, Zhou SH, Rackwitz F, Stolle DF (2021) Vibro-fluidization of sand under coupled static loading and high-frequency cyclic loading. Can Geotech J. https://doi.org/10.1139/cgj-2020-0664
16. Dewoolkar MM, Santichaianant K, Ko HY (2007) Centrifuge modeling of granular soil response over active circular trapdoors. Soils Found 47(5):931–945
17. Di HG, Zhou SH, Yao XP, Tian ZY (2021) In situ grouting tests for differential settlement treatment of a cut-and-cover metro tunnel in soft soils. Bull Eng Geol Environ 80:6415–6427. https://doi.org/10.1007/s10064-021-02276-5
18. Evans CH (1983) An examination of arching in granular soils. S.M. thesis, Department of Civil Engineering, MIT, Cambridge, MA
19. Fang HY, Li B, Wang FM, Wang YK, Cui C (2018) The mechanical behaviour of drainage pipeline under traffic load before and after polymer grouting trenchless repairing. Tunn Undergr Space Technol 74:185–194
20. Fu LL, Zhou SH, Guo PJ, Wang S, Lu Z (2019) Induced force chain anisotropy of cohesionless granular materials during biaxial compression. Granul Matter 21(3):52. https://doi.org/10.1007/s10035-019-0899-1
21. Gong QM, Zhao Y, Zhou JH, Zhou SH (2018) Uplift resistance and progressive failure mechanisms of metro shield tunnel in soft clay. Tunn Undergr Space Technol 82:222–234
22. Han J, Gabr MA (2002) Numerical analysis of geosynthetic reinforced and pile-supported earth platforms over soft soil. J Geotech Geoenviron Eng 128(1):44–53
23. Han J, Wang F, Al-Naddaf M, Xu C (2017) Progressive development of two-dimensional soil arching with displacement. Int J Geomech 17(12):04017112. https://doi.org/10.1061/(ASCE)GM.1943-5622.0001025
24. Iglesia GR, Einstein HH, Whitman RV (1999) Determination of vertical loading on underground structures based on an arching evolution concept. In: Geo-engineering for underground facilities (ASCE), pp 495–506
25. Iglesia GR, Einstein HH, Whitman RV (2014) Investigation of soil arching with centrifuge tests. J Geotech Geoenviron Eng 140(2):1–13
26. Khatami H, Deng A, Jaksa M (2019) An experimental study of the active arching effect in soil using the digital image correlation technique. Comput Geotech 108:183–196
27. Khatami H, Deng A, Jaksa M (2020) Passive arching in rubberised sand backfills. Can Geotech J 57:549–567
28. Khatami H, Deng A, Jaksa M (2020) The arching effect in rubber–sand mixtures. Geosynth Int 27(4):432–450

29. Khosravi MH, Takemura J, Pipatpongsa T (2013) Experimental analysis of earth pressure against rigid retaining walls under translation mode. Geotechnique 63(12):1020–1028
30. Kirsch A (2010) Experimental investigation of the face stability of shallow tunnels in sand. Acta Geotech 5(1):43–62
31. Lee CJ, Wu BR, Chen HT, Chiang KH (2006) Tunnel stability and arching effects during tunnelling in soft clayey soil. Tunn Undergr Space Technol 21:119–132
32. Lee J, Kwon O, Kim I, Kim G, Lee J (2019) Cyclic pullout behavior of helical anchors for offshore floating structures under inclined loading condition. Appl Ocean Res 92:101937. https://doi.org/10.1016/j.apor.2019.101937
33. Lin XT, Chen RP, Wu HN, Meng FY, Su D (2022) A composite function model for predicting the ground reaction curve on a trapdoor. Comput Geotech 141(2):104496
34. Liu W, Zhao Y, Shi PX, Li JY, Gan PL (2018) Face stability analysis of shield driven tunnels shallowly buried in dry sand using 1 g large-scale model tests. Acta Geotech 13(3):693–705
35. Lu W, Miao L (2015) A simplified 2-D evaluation method of the arching effect for geosynthetic-reinforced and pile-supported embankments. Comput Geotech 65:97–103
36. Paik KH, Salgado R (2003) Estimation of active earth pressure against rigid retaining walls considering arching effects. Geotechnique 53(7):643–653
37. Peerun MI, Ong DEL, Choo CS, Cheng WC (2020) Effect of interparticle behavior on the development of soil arching in soil-structure interaction. Tunn Undergr Space Technol. https://doi.org/10.1016/j.tust.2020.103610
38. Qiu G, Grabe J (2012) Active earth pressure shielding in quay wall constructions: numerical modeling. Acta Geotech 7(4):343–355
39. Roy K, Hawlader B, Kenny S, Moore L (2018) Uplift failure mechanisms of pipes buried in dense sand. Int J Geomech 18(8):04018087. https://doi.org/10.1061/(ASCE)GM.1943-5622.0001226
40. Shukla SK, Gaurav S, Sivakugan N (2009) A simplified extension of the conventional theory of arching in soils. Int J Geotech Eng 3(3):353–359
41. Smith CC (2012) Limit loads for a shallow anchor/trapdoor embedded in a non-associative coulomb soil. Geotechnique 62(7):563–571
42. Tang SB, Tang CA (2012) Numerical studies on tunnel floor heave in swelling ground under humid conditions. Int J Rock Mech Min Sci 55:139–150
43. Terzaghi K (1936) Stress distribution in dry and in saturated sand above a yielding trapdoor. In: Proceedings of 1st international conference on soil mechanics and foundation engineering, pp 307–311
44. Terzaghi K (1943) Theoretical soil mechanics. Wiley, New York
45. Vardoulakis I, Graf B, Gudehus G (1981) Trap-door problem with dry sand: a statical approach based upon model test kinematics. Int J Numer Anal Methods Geomech 5:57–78
46. Van Eekelen SJ, Bezuijen A, Oung O (2003) Arching in piled embankments; experiments and design calculations. In: Proceedings of foundations: innovations, observations, design and practice, Dundee, pp 885–894
47. Wang J, Haigh SK, Forrest G, Thusyanthan NI (2012) Mobilization distance for upheaval buckling of shallowly buried pipelines. J Pipeline Syst Eng 3(4):106–114
48. Wang L, Leshchinsky B, Evans TM, Xie Y (2017) Active and passive arching stresses in c'-φ' soils: a sensitivity study using computational limit analysis. Comput Geotech 84:47–57
49. Yamamuro JA, Abrantes AE, Lade VL (2011) Effect of strain rate on the stress-strain behavior of sand. J Geotech Geoenviron Eng (ASCE) 137(12):1169–1178
50. Yao QY, Di HG, Ji C, Zhou SH (2020) Ground collapse caused by shield tunneling in sandy cobble stratum and its control measures. Bull Eng Geol Environ 2:1–16
51. Zhao Y, Gong QM, Tian ZY, Zhou SH, Jiang H (2019) Torque fluctuation analysis and penetration prediction of EPB TBM in rock–soil interface mixed ground. Tunn Undergr Space Technol. https://doi.org/10.1016/j.tust.2019.103002
52. Zhao Y, Gong QM, Wu YJ, Tian ZY, Zhou SH, Fu LL (2021) Progressive failure mechanism in granular materials subjected to an alternant active and passive trapdoor. Transp Geotech. https://doi.org/10.1016/j.trgeo.2021.100529
53. Zhao Y, Gong QM, Wu YJ, Zornberg JG, Tian ZY, Zhang X (2021) Evolution of active arching in granular materials: Insights from load, displacement, strain, and particle flow. Powder Technol 384:160–175. https://doi.org/10.1016/j.powtec.2021.02.011
54. Zhou SH, Xiao JH, Di HG, Zhu Y (2018) Differential settlement remediation for a new shield metro tunnel in soft soils using corrective grouting method: case study. Can Geotech J 55(12):1877–1887
55. Zhu B, Jardine RJ, Foray P (2011) The use of miniature soil stress measuring cells in laboratory applications involving stress reversals. Soils Found 49(5):675–688
56. Zhu JF, Xu RQ, Liu GB (2014) Analytical prediction for tunnelling-induced ground movements in sands considering disturbance. Tunn Undergr Space Technol 41:165–175